EUROPEAN ORGANISATION FOR NUCLEAR RESEARCH (CERN)

Submitted to: JHEP

CERN-EP-2022-132
28th September 2022

Search for direct pair production of sleptons and charginos decaying to two leptons and neutralinos with mass splittings near the W-boson mass in $\sqrt{s} = 13\,\text{TeV}$ pp collisions with the ATLAS detector

The ATLAS Collaboration

A search for the electroweak production of pairs of charged sleptons or charginos decaying into two-lepton final states with missing transverse momentum is presented. Two simplified models of R-parity-conserving supersymmetry are considered: direct pair-production of sleptons ($\tilde{\ell}\tilde{\ell}$), with each decaying into a charged lepton and a $\tilde{\chi}_1^0$ neutralino, and direct pair-production of the lightest charginos ($\tilde{\chi}_1^\pm\tilde{\chi}_1^\mp$), with each decaying into a W-boson and a $\tilde{\chi}_1^0$. The lightest neutralino ($\tilde{\chi}_1^0$) is assumed to be the lightest supersymmetric particle (LSP). The analyses target the experimentally challenging mass regions where $m(\tilde{\ell}) - m(\tilde{\chi}_1^0)$ and $m(\tilde{\chi}_1^\pm) - m(\tilde{\chi}_1^0)$ are close to the W-boson mass ('moderately compressed' regions). The search uses 139 fb^{-1} of $\sqrt{s} = 13$ TeV proton–proton collisions recorded by the ATLAS detector at the Large Hadron Collider. No significant excesses over the expected background are observed. Exclusion limits on the simplified models under study are reported in the ($\tilde{\ell}$, $\tilde{\chi}_1^0$) and ($\tilde{\chi}_1^\pm$, $\tilde{\chi}_1^0$) mass planes at 95% confidence level (CL). Sleptons with masses up to 150 GeV are excluded at 95% CL for the case of a mass-splitting between sleptons and the LSP of 50 GeV. Chargino masses up to 140 GeV are excluded at 95% CL for the case of a mass-splitting between the chargino and the LSP down to about 100 GeV.

1 Introduction

Weak-scale supersymmetry (SUSY) [1–6] is a theoretical extension of the Standard Model (SM) which can solve the fine-tuning problem through the addition of a new fermionic/bosonic supersymmetric partner to each boson/fermion in the SM. In SUSY models with R-parity conservation [7], SUSY particles must be produced in pairs and the lightest supersymmetric particle (LSP) is stable and weakly interacting, thus being a candidate for dark matter [8, 9].

The SUSY particle production cross-sections at the Large Hadron Collider (LHC) are highly dependent on their masses. Squarks and gluinos are strongly produced and have significantly larger production cross-sections than non-coloured SUSY particles of equal masses, such as the sleptons (superpartners of the SM leptons) and the electroweakinos (the higgsino, wino and bino superpartners of the SM Higgs boson and electroweak gauge bosons). The electroweakinos mix to form chargino ($\tilde{\chi}_i^{\pm}, i = 1, 2$) and neutralino ($\tilde{\chi}_j^0, j = 1, 2, 3, 4$) mass eigenstates, where the states are ordered by increasing values of their mass.

The presence of light scalar partners of the SM leptons just above the mass of the LSP is still not excluded in an interesting, but experimentally challenging, area in the $m(\tilde{\ell})$–$m(\tilde{\chi}_1^0)$ plane. In particular, electroweak-scale SUSY with light smuons (superpartners of the SM muons) and a light LSP can explain the $(g-2)_\mu$ anomaly [10, 11] through additional loop corrections. The $(g-2)_\mu$ anomaly favours the mass region in the $m(\tilde{\mu})$–$m(\tilde{\chi}_1^0)$ plane that is 'moderately compressed' or 'compressed' (i.e. the region where the mass splitting $m(\tilde{\mu}) - m(\tilde{\chi}_1^0)$ is close to, or smaller than, the W-boson mass) for small $\tan\beta$ values[1] [12]. For small $\tan\beta$, results from LEP and previous LHC searches [13] excluded portions of this mass region, but an important part of it is still not ruled out. This search extends the sensitivity to light smuons beyond that reached by LEP and previous LHC searches.

The analyses presented in this paper target the direct production of slepton pairs decaying into the LSP via the emission of a charged lepton, and the direct production of $\tilde{\chi}_1^+\tilde{\chi}_1^-$, where each chargino decays to the LSP via the emission of a W-boson, which decays leptonically. A signature with two opposite-charge leptons (electrons and/or muons), $E_{\mathrm{T}}^{\mathrm{miss}}$ (defined as the magnitude of the missing transverse momentum $\mathbf{p}_{\mathrm{T}}^{\mathrm{miss}}$) and low hadronic activity is considered. A moderately compressed mass spectrum is targeted.

A previous search [14] by ATLAS considered the same models and signature. The search exploited the full ATLAS Run 2 data set, but it was optimized to target the phase-space with a large mass difference between the chargino or slepton and the LSP. The event selection was based on the two-lepton invariant mass, the $E_{\mathrm{T}}^{\mathrm{miss}}$, the $E_{\mathrm{T}}^{\mathrm{miss}}$ significance [15], a veto against b-tagged jets (i.e. those originating from b-quarks), and a requirement of less than two light jets. Finally, a shape-fitting technique was applied, exploiting several bins of the m_{T2} distribution.[2]

The new searches in this paper complement previous ones, extending the sensitivity in the experimentally challenging phase-space regions with mass splittings $m(\tilde{\ell}) - m(\tilde{\chi}_1^0)$ and $m(\tilde{\chi}_1^{\pm}) - m(\tilde{\chi}_1^0)$ close to the W-boson mass, which result in topologies very similar to those of SM processes. The areas of parameter space excluded by these results extend beyond those excluded by previous searches by ATLAS [14, 16, 17] and CMS [18–23] in the same channels. The gain in sensitivity is due to a dedicated analysis strategy for each of the two signal scenarios considered. Since the slepton signal presents only a same-flavour lepton-pair signature, the SM background is estimated with a data-driven technique using events with two leptons of different flavour and opposite-sign electric charge.

[1] In the Minimal Supersymmetric Standard Model (MSSM) $\tan\beta$ is defined as the ratio of the vacuum expectation values of the two complex Higgs doublets.

[2] The m_{T2} variable is defined in Section 6.2

In the chargino search, the signal results in both same-flavour and different-flavour lepton pairs and the topology of the signal is close to the SM WW process. In this case, a machine-learning technique is used, based on boosted decision trees specifically trained on signal samples with $m(\tilde{\chi}_1^{\pm}) - m(\tilde{\chi}_1^0)$ around the W-boson mass.

This paper is structured as follows. Section 2 and Section 3 describe the signal scenarios considered in these searches and the ATLAS detector, respectively. The data and simulated Monte Carlo (MC) samples used in the analyses, along with the trigger selections, are detailed in Section 4. Section 5 describes the physics object definitions. The search strategies and the SM background estimations are discussed in Sections 6 and 7, respectively. The experimental and theoretical systematic uncertainties considered in the two searches are documented in Section 8. Finally, the results and their statistical interpretations are presented in Section 9, followed by the conclusion in Section 10.

2 SUSY scenarios

The design of the analyses and the interpretation of the results are based on simplified models [24–26], where the masses of relevant sparticles (in this case the $\tilde{\ell}$, $\tilde{\chi}_1^{\pm}$ and $\tilde{\chi}_1^0$) are the only free parameters and all the other sparticles are assumed to be heavy and decoupled.

In models with direct $\tilde{\ell}\tilde{\ell}$ production (Figure 1(a)), each slepton decays into a charged lepton and a bino-like $\tilde{\chi}_1^0$ with a 100% branching ratio. Only $\tilde{e}$ and $\tilde{\mu}$ are considered in these models, and different assumptions about the masses of the superpartners of the left-handed and right-handed charged leptons, $\tilde{e}_{\mathrm{L}}$, $\tilde{e}_{\mathrm{R}}$, $\tilde{\mu}_{\mathrm{L}}$ and $\tilde{\mu}_{\mathrm{R}}$, are considered. Lepton flavour is conserved in all models.

The $\tilde{\chi}_1^{\pm}$ is assumed to be wino-like and decay into a bino-like $\tilde{\chi}_1^0$ via emission of a W-boson, which may decay into an electron or muon plus neutrino(s) either directly or through the emission of a leptonically decaying τ-lepton (Figure 1(b)).

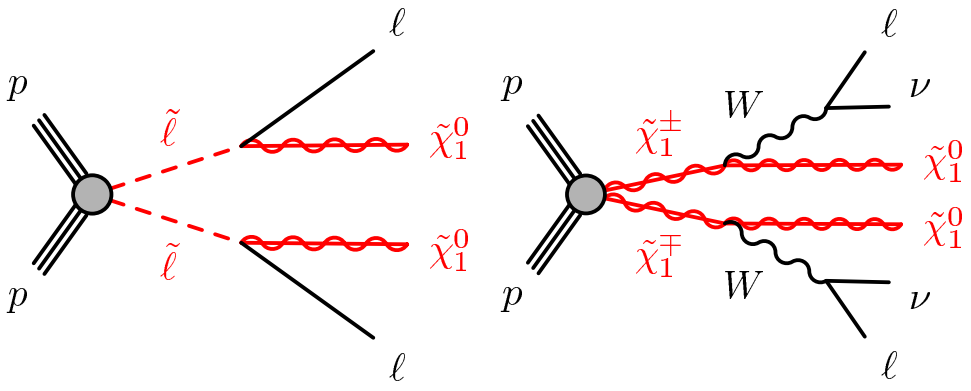

Figure 1: Diagrams of the supersymmetric simplified models considered, with two charged leptons plus weakly interacting particles in the final state: (a) slepton pair production and (b) $\tilde{\chi}_1^+\tilde{\chi}_1^-$ production with W-boson-mediated decays. Only $\tilde{e}$ and $\tilde{\mu}$ are included in the slepton model. In the final state, ℓ stands for an electron or muon, which can be produced directly or, in the case of (b), via a leptonically decaying τ-lepton along with additional neutrinos.

3 ATLAS detector

The ATLAS detector [27] at the LHC is a multipurpose particle detector with a forward–backward symmetric cylindrical geometry and an almost complete coverage in solid angle around the collision point.[3] It consists of an inner tracking detector surrounded by a thin superconducting solenoid providing a 2 T axial magnetic field, electromagnetic and hadron calorimeters, and a muon spectrometer.

The inner-detector (ID) system covers the pseudorapidity range $|\eta| < 2.5$. It consists of a high-granularity silicon pixel tracker, a silicon microstrip tracker, and a straw-tube transition-radiation tracker, which enables radially extended track reconstruction up to $|\eta| = 2.0$ and provides electron identification information. The insertable B-layer (IBL) [28, 29], installed before Run 2, typically records the innermost hit on a track.

The calorimeter system covers the pseudorapidity range $|\eta| < 4.9$. Lead/liquid-argon (LAr) sampling calorimeters provide electromagnetic (EM) energy measurements with high granularity within the region $|\eta| < 3.2$. An iron/scintillator-tile hadron calorimeter covers the central pseudorapidity range $|\eta| < 1.7$. The endcap and forward regions are instrumented with LAr calorimeters for EM and hadronic energy measurements.

The muon spectrometer (MS) surrounds the calorimeters and incorporates three large air-core toroidal superconducting magnets with eight coils each, providing a field integral ranging between 2.0 and 6.0 Tm across most of the detector. It comprises a system of precision tracking chambers measuring the deflection of muons in the magnetic field and fast detectors for triggering. The precision chamber system covers the region $|\eta| < 2.7$, while the muon trigger system covers the range $|\eta| < 2.4$.

A two-level trigger system is used to select events. The first-level (L1) trigger is implemented in hardware and accepts events at a maximum rate of 100 kHz using a subset of detector information. It is followed by a software-based high-level trigger (HLT), which reduces the accepted event rate to 1 kHz on average depending on the data-taking conditions, selecting interesting events with algorithms accessing the full detector information [30, 31]. An extensive software suite [32] is used in the reconstruction and analysis of real and simulated data, in detector operations, and in the trigger and data acquisition systems of the experiment.

4 Data and simulated event samples

The data set used in these analyses was collected by the ATLAS detector in pp collisions provided by the LHC during Run 2 from 2015 to 2018. The beams collided at a centre-of-mass energy of $\sqrt{s} = 13$ TeV and with a minimum separation of 25 ns between consecutive proton bunch crossings. The average number $\langle\mu\rangle$ of additional pp interactions per bunch crossing (pile-up) ranged from 14 in 2015 to about 38 in 2017–2018. After data-quality requirements [33], applied to ensure that all parts of the detector were operational during data-taking, the data sample amounts to a total integrated luminosity of 139 fb^{-1}. The uncertainty in the combined 2015–2018 integrated luminosity is 1.7% [34], obtained using the LUCID-2 detector [35] for the primary luminosity measurements.

[3] ATLAS uses a right-handed coordinate system with its origin at the nominal interaction point (IP) in the centre of the detector and the z-axis along the beam pipe. The x-axis points from the IP to the centre of the LHC ring, and the y-axis points upwards. Cylindrical coordinates (r, ϕ) are used in the transverse plane, ϕ being the azimuthal angle around the z-axis. The pseudorapidity is defined in terms of the polar angle θ as $\eta = -\ln\tan(\theta/2)$. Rapidity is defined as $y = (1/2)\ln[(E + p_z)/(E - p_z)]$, where E and p_z denote the energy and the component of the particle momentum along the beam direction, respectively.

Candidate events were selected by various single-electron or single-muon triggers [36, 37]. The transverse momentum (p_{T}) thresholds of the single-lepton triggers were raised as the luminosity increased during Run 2. They were in the range 20–120 GeV for data collected in 2015, 24–300 GeV for data collected in 2016, and 26–300 GeV for data collected in 2017 and 2018. Higher p_{T} requirements were applied to the lepton involved in the trigger decision during the offline lepton selection to ensure that trigger efficiencies are constant in the relevant phase-space.

MC generators were used to simulate samples of collision events, which model the expected kinematics of the investigated signal and SM background processes. For background processes, the detector response was simulated using the full modelling of the ATLAS detector [38] in GEANT4 [39], while for the signal samples a faster version of the simulation was used, which relies on a parameterization for the response of the calorimeters and on GEANT4 for the other components of the detector [38]. The effect of pile-up was modelled by overlaying the hard-scatter events with simulated inelastic pp events generated with PYTHIA 8.186 [40] and EVTGEN [41], using the NNPDF2.3LO set of parton distribution functions (PDF) [42] and the A3 set of tuned parameters [43]. The MC samples were reweighted so that the distribution of the average number of interactions per bunch crossing reproduces the observed distribution in the data. All simulated events were processed with the same trigger, reconstruction and identification algorithms as the data. Correction factors were applied to the simulated event samples to account for differences between data and simulation in the jet and lepton reconstruction efficiencies, energy scales, and energy resolutions, and in the lepton trigger efficiency [44, 45] and jet b-tagging efficiency [46].

Table 1 gives a detailed summary of all SM background samples used in the analyses. It lists the generators, the PDF sets, the sets of underlying-event and hadronisation parameter values (tune) for the parton shower, and the order of the cross-section computation in α_{s}. Further information about ATLAS simulations of $t\bar{t}$, single-top (Wt), multiboson and boson-plus-jet processes can be found in the relevant public notes [47–50].

Table 1: Simulated background event samples with the corresponding matrix element and parton shower (PS) generators, cross-section order in α_{s} used to normalize the event yield, underlying-event tune and the generator PDF sets used. For diboson, triboson and $t\bar{t}$+V samples, $V = W, Z$. Diboson samples also include Higgs boson contributions. 'Default' refers to the SHERPA generator's default tune.

Physics process	Generator	Parton shower	Normalization	Tune	PDF (generator)	PDF (PS)
$t\bar{t}$	POWHEG BOX v2 [51–54]	PYTHIA 8.230 [55]	NNLO+NNLL [56–62]	A14 [63]	NNPDF3.0NLO [64]	NNPDF2.3LO [42]
Single-top (Wt)	POWHEG BOX v2 [52–54, 65]	PYTHIA 8.230	NLO+NNLL [66, 67]	A14	NNPDF3.0NLO	NNPDF2.3LO
Diboson VV	SHERPA 2.2.1, 2.2.2 [68]	SHERPA 2.2.1, 2.2.2 [69, 70]	NLO [71–74]	Default [49]	NNPDF3.0NNLO [64]	NNPDF3.0NNLO
Triboson VVV	SHERPA 2.2.2	SHERPA 2.2.2	NLO	Default	NNPDF3.0NNLO	NNPDF3.0NNLO
$t\bar{t}$+V	MADGRAPH5_AMC@NLO 2.3.3 [75]	PYTHIA 8.210 [55]	NLO [75]	A14	NNPDF3.0NLO	NNPDF2.3LO
$t\bar{t}$+H	POWHEG BOX v2 [51–54, 76]	PYTHIA 8.230	NLO	A14	NNPDF3.0NLO	NNPDF2.3LO
$t\bar{t}$+WW	MADGRAPH5_AMC@NLO 2.2.2	PYTHIA 8.186 [40]	NLO [75]	A14	NNPDF2.3LO	NNPDF2.3LO
$t\bar{t}$+WZ	MADGRAPH5_AMC@NLO 2.3.3	PYTHIA 8.212 [55]	NLO [75]	A14	NNPDF2.3LO	NNPDF2.3LO
tZ, $t\bar{t}t\bar{t}$, $t\bar{t}t$	MADGRAPH5_AMC@NLO 2.3.3	PYTHIA 8.230	NLO [75]	A14	NNPDF3.0NLO	NNPDF2.3LO
$Z/\gamma^*(\to \ell\ell)$+jets	SHERPA 2.2.1 [68]	SHERPA 2.2.1 [70]	NNLO [77]	Default	NNPDF3.0NNLO	NNPDF3.0NNLO
$H \to \tau\tau$	POWHEG BOX v2 [52, 53, 78–80]	PYTHIA 8.2 [55]	NNLO [81–84]	AZNLO [85]	NNPDF3.0NLO	PDF4LHC15NNLO [86]

The SUSY signal samples were generated from leading-order (LO) matrix elements with up to two extra partons, using MADGRAPH v2.6.1 [87] for direct $\tilde{\ell}\tilde{\ell}$ production and MADGRAPH v2.6.2 [87] for $\tilde{\chi}_1^+\tilde{\chi}_1^- \to W^+\tilde{\chi}_1^0 W^-\tilde{\chi}_1^0$, interfaced with PYTHIA 8.244 [55] and PYTHIA 8.212 [55] respectively, with the A14 set of tuned parameters [63], for the modelling of the SUSY decay chain, parton showers, hadronization and underlying event. In order to include spin correlation effects in off-shell W-boson decays, MADSPIN [88] was used in the event generation for mass-splittings between the chargino and LSP smaller than 100 GeV. Parton luminosities were provided by the NNPDF2.3LO PDF set [42]. Jet–parton matching followed the CKKW-L prescription [89], with a matching scale set to one quarter of the pair-produced superpartner mass for the slepton model and to 15 GeV for the chargino model. Signal cross-sections were calculated to

next-to-leading order (NLO) in α_s, with resummation of soft gluon emission at next-to-leading-logarithm (NLL) accuracy [90–96]. The nominal cross-sections and their uncertainties were taken from an envelope of cross-section predictions using different PDF sets and factorization and renormalization scales, as described in Ref. [97]. The cross-section for $\tilde{\chi}_1^+\tilde{\chi}_1^-$ production, for $m(\tilde{\chi}_1^\pm) = 150$ GeV, is 2.61 ± 0.14 pb, while the cross-section for $\tilde{\ell}\tilde{\ell}$ production, for $m(\tilde{\ell}) = 150$ GeV, is 63.3 ± 3.3 fb for each generation of left-handed sleptons and 23.3 ± 1.4 fb for each generation of right-handed sleptons.

5 Object reconstruction

Candidate events are required to have at least one pp interaction vertex with a minimum of two associated tracks, each with $p_T > 500$ MeV. In events with multiple vertices, the primary vertex is defined as the one with the highest scalar sum of the squared transverse momenta of associated tracks.

The leptons selected for the analyses are classified as baseline or signal leptons using an increasingly stringent set of quality and kinematic selection criteria. The signal leptons are a subset of the baseline leptons. Baseline objects are used in the calculation of missing transverse momentum, to resolve ambiguities between the analysis objects in the event and in the fake/non-prompt (FNP) lepton background estimation described in Section 7. Signal leptons are used for the final event selection.

Baseline electron candidates are reconstructed using three-dimensional clusters of energy deposits in the electromagnetic calorimeter that are matched to an ID track. They are required to pass a *Loose* likelihood-based identification requirement [44] with an additional condition on the number of hits in the pixel detector's innermost layer, and to have $p_T > 9$ GeV and $|\eta| < 2.47$. The tracks associated with baseline electron candidates are required to be within $|z_0 \sin\theta| = 0.5$ mm of the primary vertex, where z_0 is the longitudinal impact parameter relative to the reconstructed primary vertex. Signal electrons are required to satisfy a *Tight* identification requirement [44] and the track associated with the signal electron is required to have $|d_0|/\sigma(d_0) < 5$, where d_0 is the transverse impact parameter relative to the primary vertex and $\sigma(d_0)$ is its uncertainty.

Baseline muon candidates are reconstructed in the pseudorapidity range $|\eta| < 2.6$ by matching MS tracks with ID tracks. They are required to have $p_T > 9$ GeV, to be within $|z_0 \sin\theta| = 0.5$ mm of the primary vertex and to satisfy the *Medium* identification requirements defined in Ref. [45], based on the numbers of hits in the different ID and MS subsystems, and on the significance of the charge-to-momentum ratio q/p. Signal muons are required to have the associated track with $|d_0|/\sigma(d_0) < 3$.

Isolation criteria are applied to signal electrons and muons in order to suppress contributions from photon conversions, semileptonic decays of heavy-flavour hadrons, or hadrons and jets wrongly identified as leptons, collectively referred as fake or non-prompt leptons. The scalar sum of the p_T of tracks inside a variable-size cone around the lepton (excluding its own track), must be less than 15% of the lepton p_T. The track isolation cone size for electrons (muons), $\Delta R = \sqrt{(\Delta\eta)^2 + (\Delta\phi)^2}$, is given by the minimum of $\Delta R = 10$ GeV$/p_T$ and $\Delta R = 0.2$ (0.3). In addition, for electrons (muons) the sum of the transverse energy of the calorimeter energy clusters in a cone of $\Delta R = 0.2$ around the lepton (excluding the energy from the lepton itself) must be less than 20% (30%) of the lepton p_T.

Jets are reconstructed from particle-flow objects [98] calibrated at the EM scale. The anti-k_t jet clustering algorithm [99] as implemented in the FastJet package [100] is used with a radius parameter $R = 0.4$. The reconstructed jets are corrected to particle level by the application of a jet energy scale (JES) and resolution (JER) calibrations, derived from 13 TeV data and simulation [101]. Only jet candidates with

$p_{\mathrm{T}} > 20\,\mathrm{GeV}$ and $|\eta| < 2.4$ are considered. To reduce the effects of pile-up, for jets with $p_{\mathrm{T}} < 60\,\mathrm{GeV}$ a significant fraction of the tracks associated with each jet are required to have an origin compatible with the primary vertex, as defined by the jet vertex tagger [102]. This requirement reduces the fraction of jets from pile-up to 1%, with an efficiency for pure hard-scatter jets of about 90%. Finally, in order to remove events impacted by detector noise and non-collision backgrounds, specific jet-quality requirements [103, 104] are applied to ensure that the efficiency of selecting jets from proton–proton collisions is above 99.5% (99.9%) for $p_{\mathrm{T}} > 20$ (100) GeV.

Jets that are likely to have originated from the hadronization of a bottom quark are flagged as 'b-jets' if they lie within $|\eta| < 2.4$ and are tagged by the DL1r algorithm [46], a multivariate discriminant based on various inputs such as track impact parameters and displaced secondary vertices. A selection that provides 85% efficiency for tagging b-jets in simulated $t\bar{t}$ events is used. The corresponding rejection factors for jets originating from c-quarks, from τ-leptons, and from light quarks and gluons in the same sample at this working point are 2, 4 and 31, respectively.

The identities of reconstructed objects may be ambiguous. To prevent single detector signatures from being identified as multiple objects, an overlap-removal procedure is applied to baseline leptons and jets in several consecutive steps:

- jet candidates within $\Delta R' = \sqrt{\Delta y^2 + \Delta\phi^2} = 0.2$ of an electron candidate, or jets with fewer than three tracks that lie within $\Delta R' = 0.4$ of a muon candidate, are removed because they mostly originate from calorimeter energy deposits from electron showers or muon bremsstrahlung;
- electrons and muons within $\Delta R' = \min(0.4, 0.04 + 10/p_{\mathrm{T}})$ of the surviving jets are discarded, to reject leptons from the decay of b- or c-hadrons;
- if an electron shares an ID track with a muon, the electron is discarded unless the muon is tagged as a minimum-ionizing particle in the calorimeter, in which case the muon is discarded.

The missing transverse momentum $\mathbf{p}_{\mathrm{T}}^{\mathrm{miss}}$ is defined as the negative vector sum of the transverse momenta of all identified baseline physics objects (electrons, photons, muons and jets), and an additional soft term including all tracks that pass basic quality requirements and are associated with the primary vertex but not with any reconstructed physics object [105]. The magnitude of $\mathbf{p}_{\mathrm{T}}^{\mathrm{miss}}$ is denoted by $E_{\mathrm{T}}^{\mathrm{miss}}$. Additionally, an 'object-based $E_{\mathrm{T}}^{\mathrm{miss}}$ significance' [15], referred to as $E_{\mathrm{T}}^{\mathrm{miss}}$ significance in this paper, helps to discriminate between events where $E_{\mathrm{T}}^{\mathrm{miss}}$ arises from undetected particles in the final state and those where it arises from poorly measured particles, the $\mathbf{p}_{\mathrm{T}}$ resolution, or identification inefficiencies. It is defined as

$$E_{\mathrm{T}}^{\mathrm{miss}}\ \text{significance} = \frac{|\mathbf{p}_{\mathrm{T}}^{\mathrm{miss}}|}{\sqrt{\sigma_{\mathrm{L}}^2(1-\rho_{\mathrm{LT}}^2)}}$$

where σ_{L} is the longitudinal component (parallel to the $\mathbf{p}_{\mathrm{T}}^{\mathrm{miss}}$) of the total transverse momentum resolution for all objects in the event and the quantity ρ_{LT} is the correlation factor between the parallel and perpendicular components of the transverse momentum resolution for each object.

6 Event selection

6.1 Preselection

The strategy for event preselection uses a common approach for the two analysis models, and is described here. Further selections, specific for each of the two target scenarios, are discussed in Sections 6.3.1 and 6.3.2.

Events are required to have exactly two oppositely charged signal leptons ℓ_1 and ℓ_2, with ℓ_1 having $p_{\mathrm{T}} > 27$ GeV (leading lepton) and ℓ_2 having $p_{\mathrm{T}} > 9$ GeV (sub-leading lepton). The invariant mass of the two leptons must satisfy $m_{\ell\ell} > 11$ GeV, in order to remove low-mass resonances.

Events are separated into two classes, 'same-flavour' (SF) events, i.e. $e^{\pm}e^{\mp}$ and $\mu^{\pm}\mu^{\mp}$, and 'different-flavour' (DF) events, i.e. $e^{\pm}\mu^{\mp}$, since they have different background compositions. SF events are required to have a dilepton invariant mass far from the Z peak, $|m_{\ell\ell} - 91\ \mathrm{GeV}| > 15$ GeV, to reduce VZ and Z+jets backgrounds. Events must also have no more than one jet ($n_{\mathrm{jet}} < 2$) and satisfy $E_{\mathrm{T}}^{\mathrm{miss}}$ significance > 3.

6.2 Kinematic variables

Final event selections are performed by separating signal from SM background using different kinematic variables. For both SUSY models in Figure 1, the stransverse mass m_{T2} [106, 107] and $\cos\theta^*_{\ell\ell}$, defined below, are among the most discriminating variables. The stransverse mass generalizes the transverse mass[4] m_{T} for symmetric event topologies where two identical particles each decay into a visible and an invisible product. In this case the individual transverse momenta of the invisible particles can no longer be directly approximated by the measured missing transverse momentum, because the information about their individual contributions to the missing transverse momentum is lost. The stransverse mass is defined as

$$m_{\mathrm{T2}}(\mathbf{p}_{\mathrm{T},1}, \mathbf{p}_{\mathrm{T},2}, \mathbf{p}_{\mathrm{T}}^{\mathrm{miss}}) = \min_{\mathbf{q}_{\mathrm{T},1}+\mathbf{q}_{\mathrm{T},2}=\mathbf{p}_{\mathrm{T}}^{\mathrm{miss}}} \left\{ \max[\ m_{\mathrm{T}}(\mathbf{p}_{\mathrm{T},1}, \mathbf{q}_{\mathrm{T},1}), m_{\mathrm{T}}(\mathbf{p}_{\mathrm{T},2}, \mathbf{q}_{\mathrm{T},2})\ ] \right\},$$

where $\mathbf{p}_{\mathrm{T},1}$ and $\mathbf{p}_{\mathrm{T},2}$ are the transverse-momentum vectors of the two leptons, and $\mathbf{q}_{\mathrm{T},1}$ and $\mathbf{q}_{\mathrm{T},2}$ are vectors with $\mathbf{p}_{\mathrm{T}}^{\mathrm{miss}} = \mathbf{q}_{\mathrm{T},1} + \mathbf{q}_{\mathrm{T},2}$. The minimization is performed over all the possible decompositions of $\mathbf{p}_{\mathrm{T}}^{\mathrm{miss}}$. The masses of the invisible particles are free parameters and are set to 100 GeV (giving m_{T2}^{100}) in the slepton search, since this choice improves the sensitivity to several signal models in the slepton mass range targeted by the analysis, and to 0 GeV (giving m_{T2}) in the chargino search. The variables m_{T2}^{100} and m_{T2}, typically having different kinematic endpoints for SUSY processes than for SM processes such as $t\bar{t}$ or WW, provide powerful discrimination between background events and some of the signals considered herein.

The angular variable $\cos\theta^*$, where θ^* is the polar angle between the incoming quark in one of the protons and the produced sparticle, is sensitive to the sparticle spin, and the cross-section behaves differently for scalar sparticles like sleptons, spin-1 sparticles or spin-1/2 sparticles. Since θ^* is not directly measurable, $\cos\theta^*_{\ell\ell} = \tanh(\Delta\eta_{\ell\ell}/2)$ is defined in terms of the pseudorapidity difference between the two leptons. In the slepton model, it is sensitive to the slepton production angle. The leptons 'inherit' some knowledge of the rapidity of their slepton parents, and the two variables $\cos\theta^*$ and $\cos\theta^*_{\ell\ell}$ are well correlated with each other [108]. Other variables providing powerful discrimination between signal events and backgrounds

[4] The transverse mass is defined as $m_{\mathrm{T}} = \sqrt{2 \cdot p_{\mathrm{T}} \cdot q_{\mathrm{T}} \cdot (1 - \cos(\Delta\phi))}$, where $\Delta\phi$ is the azimuthal angle between the particles with transverse momenta $\mathbf{p}_{\mathrm{T}}$ and $\mathbf{q}_{\mathrm{T}}$.

such as $t\bar{t}$ or VV ($V = W, Z$) are the azimuthal angular separations between the two leptons, $\Delta\phi_{\ell,\ell}$, between $\mathbf{p}_{\mathrm{T}}^{\mathrm{miss}}$ and the leading lepton, $\Delta\phi_{p_{\mathrm{T}}^{\mathrm{miss}},\ell_1}$, and between $\mathbf{p}_{\mathrm{T}}^{\mathrm{miss}}$ and the sub-leading lepton, $\Delta\phi_{p_{\mathrm{T}}^{\mathrm{miss}},\ell_2}$. The distributions of these variables are affected by the presence of jets in the event. For example, in slepton pair production in the absence of jets, the sleptons are expected to be produced back to back in the azimuthal plane, and the leptons coming from their decays to be well separated there. The most energetic $\tilde{\chi}_1^0$ and the sub-leading lepton are expected to come from the same slepton, so the $\mathbf{p}_{\mathrm{T}}^{\mathrm{miss}}$ vector is expected to be well separated from the $\mathbf{p}_{\mathrm{T}}^{\ell_1}$ direction.

Another exploited variable is the magnitude of $\mathbf{p}_{\mathrm{T,boost}}^{\ell\ell}$ ($p_{\mathrm{T,boost}}^{\ell\ell}$), the vector sum of the $\mathbf{p}_{\mathrm{T}}$ of the two leptons and $\mathbf{p}_{\mathrm{T}}^{\mathrm{miss}}$. It can be interpreted as the magnitude of the vector sum of all the transverse hadronic activity in the event. In both of the analysed SUSY scenarios, in absence of jets, $p_{\mathrm{T,boost}}^{\ell\ell}$ is expected to have low values due to the p_{T} balance of the system. The azimuthal separation between $\mathbf{p}_{\mathrm{T}}^{\mathrm{miss}}$ and $\mathbf{p}_{\mathrm{T,boost}}^{\ell\ell}$ is defined as $\Delta\phi_{\mathrm{boost}}$.

6.3 Signal regions

Dedicated signal-enriched regions (SRs) are defined for each signal scenario, optimized individually for benchmark signal models by maximizing the discovery significance. The selection requirements for the signal regions are explained in the following for the slepton and chargino scenarios. In both cases, they target signal models with a moderate mass difference between slepton/chargino and neutralino, up to ~ 150 GeV.

6.3.1 Slepton model

The event selection which targets the slepton model requires a SF opposite-charge (SFOS) lepton pair, $E_{\mathrm{T}}^{\mathrm{miss}}$ coming from the LSPs, and low hadronic activity apart from initial-state radiation (ISR) or pile-up. No dedicated selection for $\tilde{e}_{\mathrm{L}}$, $\tilde{e}_{\mathrm{R}}$, $\tilde{\mu}_{\mathrm{L}}$ or $\tilde{\mu}_{\mathrm{R}}$ is performed. After the preselection, only events with $n_{b\text{-tagged jets}} = 0$, i.e. the number of jets identified as b-jets by the DL1r algorithm, are retained, in order to reduce the $t\bar{t}$ and single-top backgrounds. Events are then further classified by the multiplicity of non-b-tagged jets (0J,1J).

Following the classification of the events, a dedicated optimization for each of the two categories is performed. A relevant difference between them is related to the requirements on $p_{\mathrm{T,boost}}^{\ell\ell}$ and $\Delta\phi_{p_{\mathrm{T}}^{\mathrm{miss}},\ell_1}$, which are no longer useful for the 1J event category since the presence of the jet implies that the $E_{\mathrm{T}}^{\mathrm{miss}}$ and the leptons' p_{T} are not balanced anymore. Then, two sets of SRs are defined: a set of exclusive SRs, 'binned' in m_{T2}^{100}, and a set of 'inclusive' SRs, to be used for model-dependent and model-independent results, respectively. The binning in m_{T2}^{100} is chosen to maximize the search sensitivity and retain a sufficient number of events in each bin, and the 'inclusive' SRs have different lower bounds on m_{T2}^{100} to enhance sensitivity to new physics with various mass scales. The definitions of these regions are shown in Table 2. Each SR is identified by the number of non-b-tagged jets (0J,1J) and the range of the m_{T2}^{100} interval.

6.3.2 Chargino model

The event selection which targets the chargino model considers both same-flavour and different-flavour opposite-charge lepton pairs in the event. After the preselection, only events with $n_{b\text{-tagged jets}} = 0$ and

Table 2: The definitions of the binned and inclusive signal regions for the slepton model. Relevant kinematic variables are defined in the text. The '0J' and '1J' labels refer to the multiplicity of non-b-tagged jets.

Signal region (SR)	SR-0J	SR-1J
$n_{b\text{-tagged jets}}$	= 0	
$E_{\mathrm{T}}^{\mathrm{miss}}$ significance	>7	
$n_{\text{non-}b\text{-tagged jets}}$	= 0	= 1
$p_{\mathrm{T}}{}^{\ell_1}$ [GeV]	> 140	> 100
$p_{\mathrm{T}}{}^{\ell_2}$ [GeV]	> 20	> 50
$m_{\ell\ell}$ [GeV]	> 11	> 60
$p_{\mathrm{T,boost}}^{\ell\ell}$ [GeV]	< 5	-
$\lvert\cos\theta^*_{\ell\ell}\rvert$	< 0.2	< 0.1
$\Delta\phi_{\ell,\ell}$	> 2.2	> 2.8
$\Delta\phi_{p_{\mathrm{T}}^{\mathrm{miss}},\ell_1}$	> 2.2	-
Binned SRs		
m_{T2}^{100} [GeV]	∈[100,105)	
	∈[105,110)	
	∈[110,115)	
	∈[115,120)	
	∈[120,125)	
	∈[125,130)	
	∈[130,140)	
	∈[140,∞)	
Inclusive SRs		
m_{T2}^{100} [GeV]	∈[100,∞)	
	∈[110,∞)	
	∈[120,∞)	
	∈[130,∞)	
	∈[140,∞)	

$n_{\text{non-}b\text{-tagged jets}} = 0$ are retained. The first requirement reduces the $t\bar{t}$ and single-top backgrounds, and the second one was observed to increase the sensitivity of the analysis. A machine-learning (ML) technique based on the Gradient Boosted Decision Tree (BDT) is exploited in the search for charginos [109]. Events passing the preselection and the requirements on the number of jets are separated into two categories, SF and DF, and for each category the signal and SM background Monte Carlo samples are split into two sets: the training set and test set. The BDT classifier is trained on the training set, and tested on the statistically independent test set. The test set is used to measure and optimize the classifier's performance depending on the parameters which are defined in the ML procedure, and to derive the final results. Signal samples with a mass-splitting between the chargino and neutralino of 90 or 100 GeV were found to be the best optimization benchmark across the signal grid. They were summed and a part was used for the training set. Multiclass classification is performed, i.e. the classifier is trained to separate events into four classes: signal, VV, top ($t\bar{t}$ and single-top) and all other backgrounds (Z/γ+jets, VVV and other minor backgrounds). For each event, the four scores BDT-signal, BDT-VV, BDT-top and BDT-other, corresponding to the four classes,

provide the probability for the event to belong to each class, and sum to one. This technique is found to be more effective than a simpler binary classification in discriminating signal from background. The set of variables used in the training was optimized in the analysis through an iterative procedure which started from a larger set of variables, removed variables one-by-one and retrained, keeping only variables whose removal caused a loss in performance. The reduced, final set of variables consists of $p_{\mathrm{T}}^{\ell_1}$, $p_{\mathrm{T}}^{\ell_2}$, $E_{\mathrm{T}}^{\mathrm{miss}}$, m_{T2}, $m_{\ell\ell}$, $\Delta\phi_{\mathrm{boost}}$, $\Delta\phi_{p_{\mathrm{T}}^{\mathrm{miss}},\ell_1}$, $\Delta\phi_{p_{\mathrm{T}}^{\mathrm{miss}},\ell_2}$, $\cos\theta^*_{\ell\ell}$ and $E_{\mathrm{T}}^{\mathrm{miss}}$ significance.

Requirements are placed on the BDT scores to define the SRs. Two additional requirements of $E_{\mathrm{T}}^{\mathrm{miss}}$ significance > 8 and $m_{\mathrm{T2}} > 50$ GeV are used in all relevant regions, in order to enhance the sensitivity of the search. Two sets of signal regions are defined: a set of exclusive SRs, 'binned' in BDT-signal to maximize model-dependent search sensitivity, and a set of 'inclusive' SRs, to be used for model-independent results, with a varying lower bound on BDT-signal. The definitions of these regions are shown in Table 3.

Table 3: The definitions of the binned and inclusive signal regions for the chargino model. Relevant variables are defined in the text. The signal regions are separated for DF and SF, except for the first inclusive SR (subsequently indicated with $\mathrm{SR}^{\text{-DF BDT-signal}\in(0.81,1]}_{\text{-SF BDT-signal}\in(0.77,1]}$), which contains DF events with BDT-signal ∈(0.81,1] and SF events with BDT-signal ∈(0.77,1].

Signal region (SR)	SR-DF	SR-SF
$n_{b\text{-tagged jets}}$	= 0	
$n_{\text{non-}b\text{-tagged jets}}$	= 0	
$E_{\mathrm{T}}^{\mathrm{miss}}$ significance	>8	
m_{T2} [GeV]	>50	
BDT-other		< 0.01
Binned SRs		
BDT-signal	∈(0.81,0.8125]	∈(0.77,0.775]
	∈(0.8125,0.815]	∈(0.775,0.78]
	∈(0.815,0.8175]	∈(0.78,0.785]
	∈(0.8175,0.82]	∈(0.785,0.79]
	∈(0.82,0.8225]	∈(0.79,0.795]
	∈(0.8225,0.825]	∈(0.795,0.80]
	∈(0.825,0.8275]	∈(0.80,0.81]
	∈(0.8275,0.83]	∈(0.81,1]
	∈(0.83,0.8325]	
	∈(0.8325,0.835]	
	∈(0.835,0.8375]	
	∈(0.8375,0.84]	
	∈(0.84,0.845]	
	∈(0.845,0.85]	
	∈(0.85,0.86]	
	∈(0.86,1]	
Inclusive SRs		
BDT-signal	∈(0.81,1]	∈(0.77,1]
	∈(0.81,1]	
	∈(0.82,1]	
	∈(0.83,1]	
	∈(0.84,1]	
	∈(0.85,1]	
		∈(0.77,1]
		∈(0.78,1]
		∈(0.79,1]
		∈(0.80,1]

7 Background estimation

The SM backgrounds can be classified into irreducible backgrounds, from processes with prompt leptons which can yield events with a final state similar to the signal, and reducible backgrounds, which contain one or more FNP leptons. Among the irreducible backgrounds, for both the slepton and chargino searches

the dominant sources are processes with top quarks or dibosons (VV).

The slepton search uses a dedicated data-driven technique to estimate some of the dominant backgrounds. This technique is based on the observation that, while the slepton decays produce events with two SFOS leptons in the final state, the decays of background processes such as $t\bar{t}$, single-top, WW and $Z(\rightarrow \tau\tau)$+jets produce opposite-sign SF or DF leptons with the same probability ('flavour-symmetric backgrounds', FSB). The DF channel (populated by the background only) can be used to predict the contribution of FSB to the SF channel (populated by the background and, potentially, by the signal).

The chargino search uses a partially data-driven technique to estimate the dominant backgrounds. Dedicated control regions (CRs), enriched in particular backgrounds, are used to normalize MC simulation yields to data. A simultaneous profile likelihood fit (described in Section 9) is used to constrain the MC yields with the observed data. The CRs are designed to be both orthogonal and similar to the SRs, whilst also having little signal contamination; this is achieved by taking the SR definitions and inverting some of the selection criteria. Dedicated validation regions (VRs) are defined to be kinematically close to CRs and SRs, and are used to assess the quality of the background estimation and its extrapolation to the SRs.

Subdominant irreducible SM background contributions arising from Drell–Yan, $t\bar{t}$+boson(s), tZ, $t\bar{t}t\bar{t}$, $t\bar{t}t$, Higgs boson, and VVV processes, jointly referred to as 'Other backgrounds' (or 'Others' in the figures), are estimated from simulation using the samples described in Section 4.

The reducible background from FNP leptons is estimated from data using the matrix method (MM) [110]. This method uses two types of leptons: 'signal' leptons, corresponding to leptons passing the final selection used in the analysis, and 'baseline' leptons, which pass a looser selection as defined in Section 5. Probabilities for prompt leptons satisfying the baseline selection to also satisfy the signal selection are measured as a function of lepton p_{T} and η in MC simulation, using control samples enriched in real leptons. Similar probabilities for FNP leptons to pass the signal selection are measured in data events dominated by leptons from the decays of heavy-flavour hadrons and from photon conversions, and in MC control samples dominated by leptons from light-flavour quark decays. The final probability is then computed by summing the FNP contributions from the different sources, with appropriate weights (w_i) which reflect the relative amount from each source, extracted from MC simulations by using event information from the generator's 'truth' record. These probabilities are used in the MM method when solving a set of equations relating the numbers of observed baseline and signal leptons to the estimated numbers of real and FNP leptons in the CRs, VRs, and SRs. To avoid double counting between the simulated samples used for background estimation and the FNP lepton background estimate provided by the MM, all simulated events containing one or more FNP leptons are removed from the background samples.

7.1 Estimation of the backgrounds in the slepton search

The number of data events with DF leptons surviving the SR selection (N_{DF}) can be used, after subtracting the FNP lepton contribution, to predict the FSB in the SF channel. Since electrons and muons have different acceptances and trigger, reconstruction, isolation and identification efficiencies, these differences must be taken into account. An efficiency correction method is applied, allowing the expected number of FSB events in the SF channel to be computed as

$$
\begin{aligned}
N_{ee}^{\text{expected}} &= 0.5 \times \frac{1}{\kappa} \times \alpha \times N_{\text{DF}} \\
N_{\mu\mu}^{\text{expected}} &= 0.5 \times \kappa \times \alpha \times N_{\text{DF}} \\
N_{\text{SF}}^{\text{expected}} &= 0.5 \times \left(\kappa + \frac{1}{\kappa}\right) \times \alpha \times N_{\text{DF}}
\end{aligned}
\tag{1}
$$

where it is assumed that efficiencies factorize for the individual leptons, the production rate of the DF events is twice that of the dimuon or dielectron events, and κ and α take into account the different muon and electron acceptances and the different muon and electron reconstruction, identification and trigger efficiencies, respectively. They are defined as

$$
\kappa = \sqrt{\frac{N_{\mu^+\mu^-}}{N_{e^+e^-}}}
$$

$$
\alpha = \frac{\sqrt{\epsilon_{\mu\mu}^{\text{trig}}\,\epsilon_{ee}^{\text{trig}}}}{\epsilon_{e\mu}^{\text{trig}}}
$$

with $N_{\mu^+\mu^-}$ and $N_{e^+e^-}$ being the numbers of dimuon and dielectron events respectively, and $\epsilon_{\mu\mu}^{\text{trig}}$, $\epsilon_{ee}^{\text{trig}}$ and $\epsilon_{e\mu}^{\text{trig}}$ the efficiencies of triggering dimuon, dielectron and electron–muon events with the trigger selection described in Section 4.

The factor κ is extracted from data in a control sample obtained by relaxing the requirements on ${p_{\text{T}}}^{\ell_1}$ and the $E_{\text{T}}^{\text{miss}}$ significance and inverting the requirement on $|\cos\theta_{\ell\ell}^{*}|$ to make it orthogonal to the SRs. The value of κ was observed to depend on the leading lepton's p_{T} in different η regions of the detector, and it is therefore parameterized as a function of ${p_{\text{T}}}^{\ell_1}$ only, $\kappa = a + b/p_{\text{T}}^{\ell_1}$. This parameterization gives a good description of the behaviour of κ in both data and MC simulation.

The factor α is computed from the global efficiencies of the trigger selection applied in the analysis, evaluated in a control sample of data events passing an independent trigger selection based on $E_{\text{T}}^{\text{miss}}$. In the η and p_{T} ranges where the two leptons satisfy the selection criteria in the SRs, the dependence of α on these kinematic variables was found to be negligible.

In order to validate the efficiency correction method, two validation regions, VR-0J and VR-1J, are defined, with the same selection as in the corresponding SR but inverting the $|\cos\theta_{\ell\ell}^{*}|$ requirement. Although VR-0J and VR-1J are subsets of the control sample used to extract the factor κ, they use different events, since in these VRs the FSB contribution is evaluated from DF events in data using Eq. (1). Figure 2 shows m_{T2}^{100} in VR-0J and VR-1J, and good agreement is observed between the data and the total estimated SM background in these distributions and in all other variables relevant for the analysis.

Finally, the FSB yields in SR-0J and SR-1J defined in Table 2 are estimated using the DF events surviving in data after imposing the selections for each SR and applying the factors κ and α on an event-by-event basis. They are reported in Table 4.

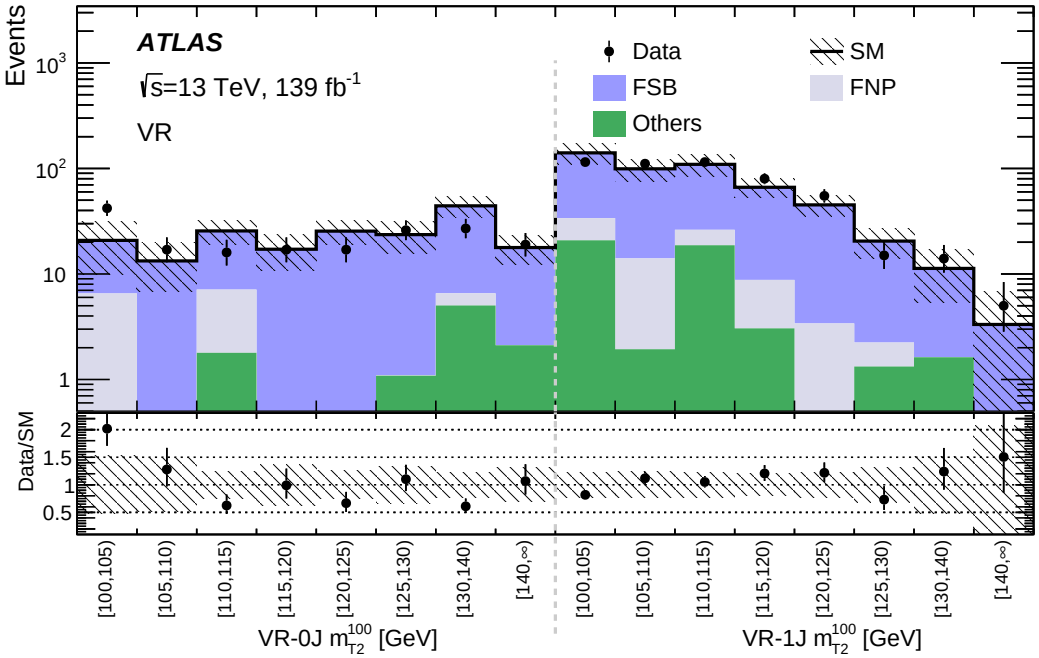

Figure 2: Distributions of m_{T2}^{100} in VR-0J and in VR-1J for data and the estimated SM backgrounds. The FSB contribution is evaluated with the data-driven efficiency correction method. The FNP lepton background is calculated using the data-driven matrix method. 'Others' include the non-dominant background sources, e.g. $t\bar{t}$+V, Higgs boson and Drell–Yan events. The shaded band represents the total uncertainty, coming from all sources, of the expected SM background. The lower panel shows the ratio of data to the SM background estimate.

Table 4: Expected flavour-symmetric background yields in SR-0J and SR-1J, estimated from surviving DF data events after imposing the selections for each SR and applying the factors κ and α on an event-by-event basis. Yields are separated for ee and $\mu\mu$ events. The uncertainties include both the statistical and systematic contributions.

SR	ee events	$\mu\mu$ events	Total
SR-0J	34.6 ± 4.9	30.2 ± 4.4	64.8 ± 9.3
SR-1J	37.1 ± 5.0	31.8 ± 4.5	68.9 ± 9.4

The irreducible SM non-flavour-symmetric background contribution in SR-0J and SR-1J is estimated directly from simulation using the samples described in Section 4.

7.2 Estimation of the backgrounds in the chargino search

The general strategy to define CRs and VRs relies on reversing the BDT-signal requirement applied to the SRs or selecting events with $n_{b\text{-tagged jets}} = 1$ for the top CR, in order to ensure orthogonality with the SRs and low signal contamination. A summary of the regions considered is given in Table 5 and the strategy is described in the following.

Table 5: Control region definitions for extracting the normalization factors for the dominant background processes in the chargino search and validation region definitions used to study the modelling of the SM backgrounds. The requirements are applied on top of the preselection. 'DF' or 'SF' refer to control/validation regions with different lepton flavour or same lepton flavour pair combinations, respectively.

Control region (CR)	CR-VV		CR-top	
$E_{\mathrm{T}}^{\mathrm{miss}}$ significance	> 8			
m_{T2} [GeV]	> 50			
$n_{\text{non-}b\text{-tagged jets}}$	$= 0$			
Leptons flavour	DF	SF	DF	SF
$n_{b\text{-tagged jets}}$	$= 0$	$= 0$	$= 1$	$= 1$
BDT-other	-	< 0.01	-	< 0.01
BDT-signal	$\in (0.2, 0.65]$	$\in (0.2, 0.65]$	$\in (0.5, 0.7]$	$\in (0.7, 0.75]$
BDT-VV	> 0.2	> 0.2	-	-
BDT-top	< 0.1	< 0.1	-	-

Validation region (VR)	VR-VV-DF	VR-VV-SF	VR-top-DF	VR-top-SF	VR-top0J-DF	VR-top0J-SF
$E_{\mathrm{T}}^{\mathrm{miss}}$ significance	> 8					
m_{T2} [GeV]	> 50					
$n_{\text{non-}b\text{-tagged jets}}$	$= 0$					
$n_{b\text{-tagged jets}}$	$= 0$	$= 0$	$= 1$	$= 1$	$= 0$	$= 0$
BDT-other	-	< 0.01	-	< 0.01	-	< 0.01
BDT-signal	$\in (0.65, 0.81]$	$\in (0.65, 0.77]$	$\in (0.7, 1]$	$\in (0.75, 1]$	$\in (0.5, 0.81]$	$\in (0.5, 0.77]$
BDT-VV	> 0.2	> 0.2	-	-	< 0.15	< 0.15
BDT-top	< 0.1	< 0.1	-	-	-	-

Two CRs are used, CR-VV to target the diboson backgrounds and CR-top to target the top-quark backgrounds ($t\bar{t}$ and Wt). The selection $E_{\mathrm{T}}^{\mathrm{miss}}$ significance > 8, $m_{\mathrm{T2}} > 50$ GeV and $n_{\text{non-}b\text{-tagged jets}} = 0$ applied in these CRs is the same as used in the SRs, in order to ensure that they and the SRs have similar kinematic phase-spaces. Upper bounds on the BDT-signal score are exploited to ensure orthogonality with the SRs and low signal contamination. Requirements on the background BDT scores are then applied to ensure that the CR is sufficiently pure in the targeted background. The $n_{b\text{-tagged jets}} = 1$ selection is used in CR-top to ensure a large top-quark background contribution. A dedicated selection is used for DF and SF events, in order to be consistent with the SR definitions. The CR selections are summarized in the first part of Table 5. The expected number of signal events in the CRs, from the considered models, is at most 5% of the total background yield.

Diboson and top-quark backgrounds are normalized to the data observed in CR-VV and CR-top in a simultaneous likelihood fit, using a normalization factor for each background (μ_{VV} and μ_{top}). The number of data events observed in each CR, as well as the predicted yield of each SM process, is shown in Table 6. For backgrounds whose normalization is extracted from the likelihood fit, the yield expected from the MC simulation is also reported. The normalization factors applied to the VV and top-quark backgrounds are found to be $\mu_{\mathrm{VV}} = 1.38 \pm 0.08$ and $\mu_{\mathrm{top}} = 1.09 \pm 0.03$, where the errors include all uncertainties described in Section 8. The shapes of kinematic distributions are well reproduced by the simulation in each CR, as shown in Figure 3.

A set of six validation regions is used to verify that the SM predictions and data agree within uncertainties

Table 6: Observed event yields and predicted background yields from the likelihood fit in the CRs for the chargino search. For backgrounds with a normalization extracted from the likelihood fit, the expected yield from the simulation before the likelihood fit is also shown. The FNP lepton background is calculated using the data-driven matrix method. 'Other backgrounds' include the non-dominant background sources, e.g. $t\bar{t}$+V, Higgs boson and Drell–Yan events. The uncertainties include both the statistical and systematic contributions.

Region	CR-VV	CR-top
Observed events	634	4468
Fitted backgrounds	634 ± 25	4470 ± 70
Fitted VV	520 ± 27	68 ± 12
Fitted $t\bar{t}$	69 ± 7	3240 ± 100
Fitted single-top	40 ± 6	1130 ± 90
Other backgrounds	$4.8^{+5.1}_{-4.8}$	29 ± 5
FNP leptons	$0.02^{+1.4}_{-0.02}$	$0.06^{+12}_{-0.06}$
Simulated VV	376	49
Simulated $t\bar{t}$	63	2974
Simulated single-top	37	1040

in regions with a phase-space kinematically close to the SRs, after performing the likelihood fit. The definitions are reported in the second part of Table 5. The regions VR-VV-DF, VR-VV-SF, VR-top-DF and VR-top-SF are designed to have an intermediate BDT-signal selection range compared to the corresponding CRs and SRs. Regions VR-top0J-DF and VR-top0J-SF are used to validate the extrapolation of the top-quark normalization factor from the region with $n_{b\text{-tagged jets}} = 1$ (CR-top) to regions with $n_{b\text{-tagged jets}} = 0$ (SRs). Furthermore, VR-top0J-DF and VR-top0J-SF are also used to validate the top-quark background estimate in regions with the same relative fraction of $t\bar{t}$ and Wt as the one expected in the SRs.

The number of observed events and the predicted background in each VR are shown in Table 7. They agree within one standard deviation except in VR-top0J-DF, where a 1.8σ discrepancy is observed. For backgrounds with a normalization extracted from the likelihood fit, the expected yield from the simulated samples before the likelihood fit is also shown. Figure 4 shows a selection of kinematic distributions for data and the estimated SM background in the validation regions defined in Table 5. Good agreement is observed in all regions.

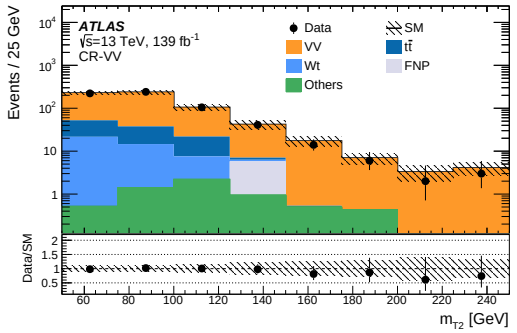

(a) m_{T2} distribution in CR-VV

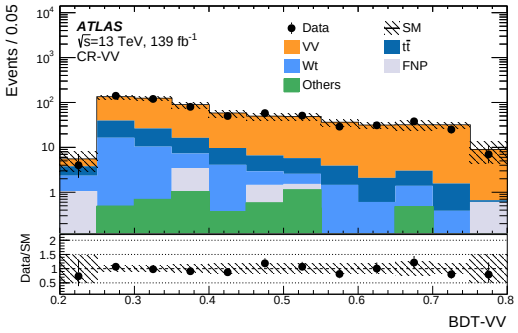

(b) BDT-VV distribution in CR-VV

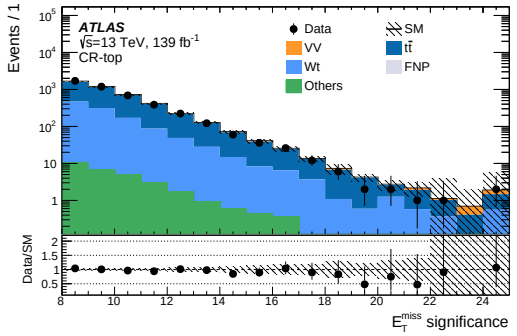

(c) $E_{\mathrm{T}}^{\mathrm{miss}}$ significance distribution in CR-top

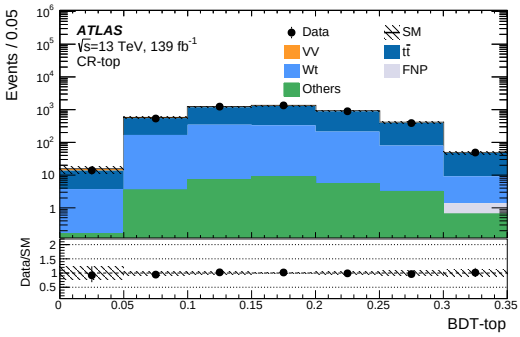

(d) BDT-top distribution in CR-top

Figure 3: Distributions of (a) m_{T2} , (b) BDT-VV in CR-VV, (c) $E_{\mathrm{T}}^{\mathrm{miss}}$ significance and (d) BDT-top in CR-top for data and the estimated SM backgrounds. The normalization factors extracted from the corresponding CRs are used to rescale the $t\bar{t}$, single-top-quark and VV backgrounds. The FNP lepton background is calculated using the data-driven matrix method. 'Others' include the non-dominant background sources, e.g. $t\bar{t}$+V, Higgs boson and Drell–Yan events. The uncertainty band includes systematic and statistical errors from all sources and the final bin in each histogram includes the overflow. The lower panels show the ratio of data to the SM background estimate.

Table 7: Observed event yields and predicted background yields in the VRs for the chargino search. For backgrounds with a normalization extracted from the likelihood fit in the CRs, the expected yield from the simulation before the likelihood fit is also shown. The FNP lepton background is calculated using the data-driven matrix method. 'Other backgrounds' include the non-dominant background sources, e.g. $t\bar{t}$+V, Higgs boson and Drell–Yan events. The uncertainties include both the statistical and systematic contributions.

Regions	VR-VV-DF	VR-VV-SF	VR-top-DF	VR-top-SF	VR-top0J-DF	VR-top0J-SF
Observed events	972	596	1910	95	810	17
Fitted backgrounds	940 ± 60	670 ± 90	1900 ± 90	101 ± 10	880 ± 40	18 ± 4
Fitted VV	730 ± 50	400 ± 50	32 ± 13	2.2 ± 2.1	427 ± 30	8.1 ± 2.6
Fitted $t\bar{t}$	116 ± 12	111 ± 11	1350 ± 50	67 ± 7	260 ± 21	5.8 ± 1.8
Fitted single-top	94 ± 19	75 ± 11	500 ± 60	27 ± 7	168 ± 18	4 ± 1
Other backgrounds	3.1 ± 1.5	70 ± 70	13.6 ± 2.5	0.8 ± 0.4	5.2 ± 1.9	0.05 ± 0.05
FNP leptons	$0.02^{+2.3}_{-0.02}$	7 ± 4	$0.03^{+5}_{-0.03}$	4.2 ± 1.3	21 ± 8	$0.05^{+0.15}_{-0.05}$
Simulated VV	527	291	23	1.6	309	5.9
Simulated $t\bar{t}$	106	102	1240	61	239	5.3
Simulated single-top	87	69	460	25	154	3.2

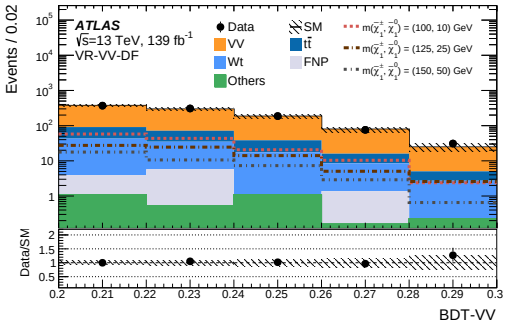

(a) BDT-VV distribution in VR-VV-DF

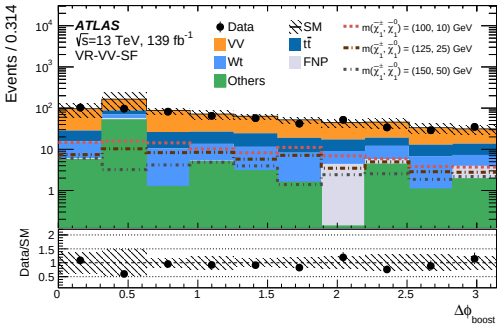

(b) $\Delta\phi_{\text{boost}}$ distribution in VR-VV-SF

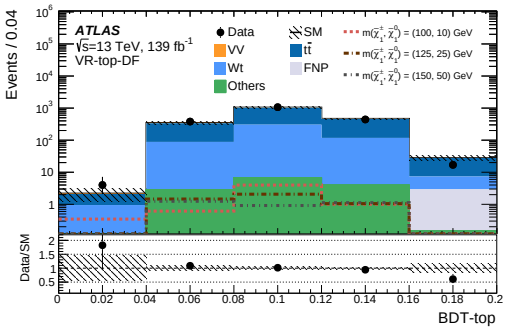

(c) BDT-top distribution in VR-top-DF

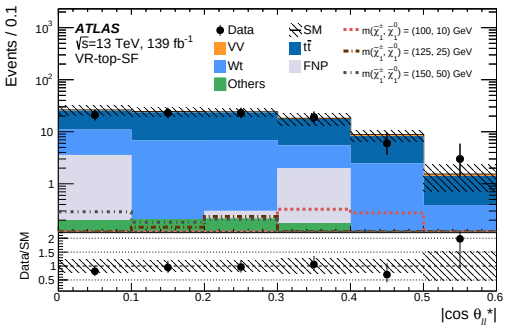

(d) $|\cos\theta^*_{\ell\ell}|$ distribution in VR-top-SF

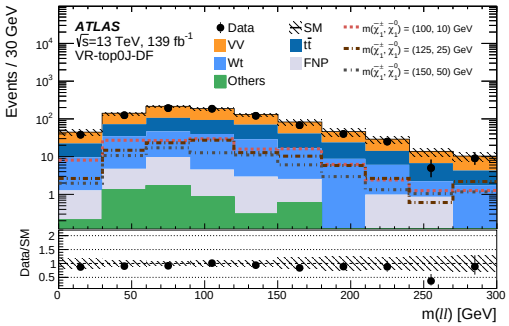

(e) $m_{\ell\ell}$ distribution in VR-top0J-DF

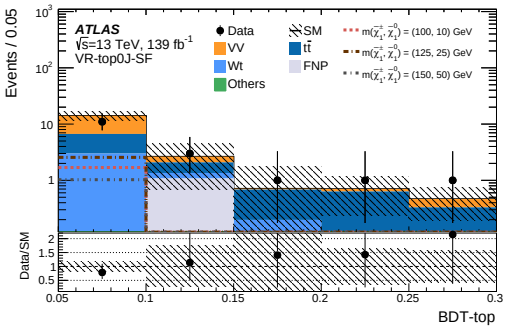

(f) BDT-top distribution in VR-top0J-SF

Figure 4: Distributions of (a) BDT-VV in VR-VV-DF, (b) $\Delta\phi_{\text{boost}}$ in VR-VV-SF, (c) BDT-top in VR-top-DF, (d) $|\cos\theta^*_{\ell\ell}|$ in VR-top-SF, (e) $m_{\ell\ell}$ in VR-top0J-DF and (f) BDT-top in VR-top0J-SF, for data and the estimated SM backgrounds. The normalization factors extracted from the corresponding CRs are used to rescale the $t\bar{t}$, single-top-quark and VV backgrounds. The FNP lepton background is calculated using the data-driven matrix method. 'Others' include the non-dominant background sources, e.g. $t\bar{t}$+V, Higgs boson and Drell–Yan events. The uncertainty band includes systematic and statistical errors from all sources and the last bin includes the overflow. Distributions for three benchmark signal points are overlaid for comparison. The lower panels show the ratio of data to the SM background estimate.

8 Systematic uncertainties

This section describes the uncertainties in the SM background predictions, while the uncertainties associated with the signal models are discussed in Section 4. The likelihood fits used for calculating the results of the two analyses consider all relevant sources of experimental and theoretical systematic uncertainty affecting the SM background estimates and the signal predictions. The major sources of uncertainty in the slepton search are related to the FSB estimation, while in the chargino search the dominant contributions come from the VV theoretical uncertainty, normalization of background processes, and uncertainty associated with the jet energy scale and resolution and with the $\mathbf{p}_{\mathrm{T}}^{\mathrm{miss}}$ soft-term scale and resolution. Statistical uncertainties associated with the simulated MC samples are also accounted for. For the chargino search, in the cases where the normalization of background processes (VV and top) are calculated using control regions, the systematic uncertainties only affect the extrapolation to the signal regions.

The jet energy scale and resolution uncertainties are calculated as a function of the p_{T} and η of the jet, and the pile-up conditions and flavour composition of the selected jet sample. They are derived using a combination of data and simulated samples, through studies including measurements of the transverse momentum balance between a jet and a reference object in dijet, Z+jets and γ+jets events [101, 111, 112]. An additional uncertainty in the modelling of $\mathbf{p}_{\mathrm{T}}^{\mathrm{miss}}$ comes from the soft-term resolution and scale [105]. Experimental uncertainties of the scale factors used to account for differences between the data and simulation in b-jet identification, lepton reconstruction efficiency and trigger efficiency are also included. The remaining experimental uncertainties include lepton energy scale and resolution, and are found to be negligible across all analysis regions.

Several sources of theoretical uncertainty in the modelling of the dominant backgrounds are considered. Modelling uncertainties affecting diboson, $t\bar{t}$, single-top (Wt) and Z+jets backgrounds are considered in the chargino search, whilst the slepton search only considers modelling uncertainties affecting the WZ/ZZ diboson processes and Z+jets, due to the data-driven background estimation method used for the flavour-symmetric backgrounds.

The diboson modelling uncertainties are calculated by varying the PDF sets [64] as well as the QCD renormalization and factorization scales used to generate the samples. Uncertainties from missing higher orders are evaluated [113] using six variations of the QCD factorization and renormalization scales in the matrix elements by factors of 0.5 and 2, avoiding variations in opposite directions. Additional uncertainties in the resummation and matching scales between the matrix element generator and parton shower are considered.

The $t\bar{t}$ background estimate is affected by modelling uncertainties associated with the parton shower modelling, the different approaches commonly used in the matching between the matrix element and the parton shower, and the modelling of initial- and final-state radiation (ISR/FSR). Uncertainties in the parton shower simulation are estimated by comparing samples generated with Powheg Box interfaced to either Pythia 8.186 or Herwig 7.04 [114, 115]. The ISR/FSR uncertainties are calculated by comparing the predictions of the nominal sample with alternative scenarios with the relevant generator parameters varied [116]. The uncertainty associated with the choice of event generator is estimated by comparing the nominal samples with samples generated with aMC@NLO interfaced to Pythia 8.186 [116]. Finally, for single-top-quark production, an uncertainty is assigned to the treatment of the interference between the Wt and $t\bar{t}$ samples. This is done by comparing the nominal sample generated using the diagram removal method with a sample generated using the diagram subtraction method [117, 118].

Table 8: Breakdown of the dominant systematic uncertainties in background estimates in the inclusive SRs requiring $m_{\mathrm{T2}}^{100} \in [100, \infty)$ GeV for the 0J and 1J selections in the slepton search. The individual uncertainties can be correlated, and do not necessarily sum in quadrature to the total background uncertainty. The percentages show the size of the uncertainty relative to the total expected background.

Region m_{T2} [GeV]	SR-0J $\in$[100,∞)	SR-1J $\in$[100,∞)
Total background expectation	76	78
MC and FSB statistical uncertainties	14%	13%
FSB estimate	9%	9%
FNP leptons	5%	4%
$Z/\gamma^*(\rightarrow \ell\ell)$+jets theoretical uncertainties	< 1%	3%
$E_{\mathrm{T}}^{\mathrm{miss}}$ modelling	2.3%	< 1%
Jet energy scale	< 1%	< 1%
Jet energy resolution	< 1%	1%
b-tagging	< 1%	< 1%
Lepton modelling	1%	< 1%
Total systematic uncertainty	17%	17%

The Z+jets background estimate is affected by QCD factorization and renormalization scale uncertainties. Uncertainties in the resummation and matching scales between the matrix element generator and parton shower are also considered.

The uncertainty in the MM estimate of the FNP background has several components. The 'real' efficiencies and the electron light-flavour fake rate (which are calculated using MC simulation) are affected by the experimental uncertainties of the scale factors applied to account for lepton trigger, identification, reconstruction and isolation efficiency differences between data and simulation. For the heavy-flavour fake rate, the effects of uncertainties in the subtraction of the prompt-lepton contamination in the control region are calculated by varying this contamination and evaluating the changes in the FNP background estimates. Finally, uncertainties in the expected composition of the FNP leptons in the signal regions are included, along with the statistical uncertainties of the 'real' efficiencies and fake rates used in the calculation.

For the slepton search, additional uncertainties associated with the data-driven background estimate of the flavour-symmetric backgrounds (FSB estimate) discussed in Section 7 are also applied. The statistical uncertainty of the DF sample is included. Uncertainties in the κ and α factors that account for the reconstruction, identification and trigger efficiency differences between muons and electrons are obtained by considering the differences between global efficiencies calculated in data and simulation. Finally, additional uncertainties are applied to account for possible changes in the results if the events are reweighted as a function of the sub-leading lepton p_{T} instead of the leading lepton p_{T}, and for the choice of fitting function for the dependence of κ on this variable. A summary of the impact of the systematic uncertainties on the background yields in the inclusive SRs requiring $m_{\mathrm{T2}}^{100} \in [100, \infty)$ GeV, after performing the likelihood fit, is shown in Table 8 for the 0J and 1J selections.

Table 9: Breakdown of the dominant systematic uncertainties in background estimates in the inclusive region $\mathrm{SR}^{\text{-DF BDT-signal}\in(0.81,1]}_{\text{-SF BDT-signal}\in(0.77,1]}$ for the chargino search. The individual uncertainties can be correlated, and do not necessarily sum in quadrature to the total background uncertainty. The percentages show the size of the uncertainty relative to the total expected background.

Region	$\mathrm{SR}^{\text{-DF BDT-signal}\in(0.81,1]}_{\text{-SF BDT-signal}\in(0.77,1]}$
Total background expectation	630
$E_{\mathrm{T}}^{\mathrm{miss}}$ modelling	9.1%
Diboson theoretical uncertainties	5.8%
Jet energy scale	5.2%
VV normalization	3.6%
Jet energy resolution	1.7%
MC statistical uncertainties	1.7%
Lepton modelling	1.2%
Top theoretical uncertainties	1%
$t\bar{t}$ normalization	1%
FNP leptons	0.8%
b-tagging	0.7%
$Z/\gamma^{*}(\rightarrow \ell\ell)$+jets theoretical uncertainties	0.04%
Total systematic uncertainty	12%

For the chargino search, a summary of the impact of the systematic uncertainties on the background yields in the inclusive region $\mathrm{SR}^{\text{-DF BDT-signal}\in(0.81,1]}_{\text{-SF BDT-signal}\in(0.77,1]}$, obtained as a combination of the integrals of all DF and SF binned regions in Table 3, is shown in Table 9 after performing the likelihood fit.

9 Results

The results of the two searches are interpreted in the context of the slepton and chargino simplified models shown in Figure 1, and as general limits on new-physics cross-sections.

The statistical interpretation of the results is performed using the HistFitter [119] framework. The likelihood is a product of Poisson probability density functions, describing the observed number of events in each CR/SR, and Gaussian distributions that describe the nuisance parameters associated with each of the systematic uncertainties. Furthermore, Poisson distributions are used for MC statistical uncertainties. Systematic uncertainties that are correlated between different samples are accounted for in the fit configuration by using the same nuisance parameter. In particular, experimental systematic uncertainties are correlated between background and signal samples for all regions. The uncertainties are applied in each of the CRs and SRs and their effect is correlated for events across all regions in the fit.

The background fit strategy differs between the two searches. The chargino search uses data in the CRs and the likelihood fit is performed to constrain the nuisance parameters of the likelihood function, which include

the background normalization factors and parameters associated with the systematic uncertainties. The slepton search uses the FSB prediction in the SRs, and the likelihood fit is used to constrain the nuisance parameters associated with the systematic uncertainties. In both cases, the results of the background fit are used to test the compatibility of the observed data and the background estimates in the inclusive SRs.

The CL_s method [120] is used to set model-independent upper limits at 95% confidence level (CL) on the visible signal cross-section σ^{obs}, defined as the cross-section times acceptance times efficiency, for processes beyond the SM. They are derived in each inclusive SR by performing a fit that includes the CRs, the observed yield in the SR as a constraint, and a signal yield in the SR as a free parameter of interest. The observed ($S^{0.95}_{obs}$) and expected ($S^{0.95}_{exp}$) limits at 95% CL on the numbers of events from processes beyond the SM in the inclusive SRs are calculated. The p_0-values, which represent the probability of the SM background alone to fluctuate to the observed number of events or higher, are also included in the results and are capped at $p_0 = 0.50$.

Exclusion limits at 95% CL are placed on the masses of the sleptons, chargino and neutralino. The CL_s prescription is also used in this case, including the data in the binned SRs in the simultaneous likelihood fit.

9.1 Results of the slepton search

The predicted number of background events obtained by applying the efficiency correction method to compute the expected number of FSB events, together with the observed data in the binned SRs defined in Table 2, are shown in Figure 5 for 0J and 1J selections. In the binned SR-0J, the expected background exceeds the observed data in two m^{100}_{T2} bins, with a local significance of about 2σ. The same behaviour is observed in these bins when using pure MC simulations to estimate the background, so the disagreement most likely arises from statistical fluctuations in data. In the binned SR-1J, there are excesses of data of about 1.5σ in two m^{100}_{T2} bins, while the expected background exceeds the observed data with a local significance of 3.5σ in one m^{100}_{T2} bin. These discrepancies are found to be strictly correlated with statistical fluctuations in the distribution of DF events in data which are used to estimate the FSB. This is observed when comparing pure MC simulations with DF data in the SRs. Furthermore, when comparing pure MC simulations with SF data in the SRs, fluctuations of the data in the opposite direction are observed. The combination of the two effects enhances the discrepancy.

The observed and predicted numbers of background events in the inclusive SRs are reported in Table 10, together with the model-independent upper limits on the visible signal cross-section σ^{obs}, the observed and expected limits at 95% CL on the number of potential beyond-the-SM events, and the p_0-values. Exclusion limits at 95% CL on the masses of the sleptons and neutralino are shown in Figure 6 for mass-degenerate $\tilde{e}_{L,R}/\tilde{\mu}_{L,R}$, bridging the gap between previous ATLAS searches and surpassing limits from LEP: sleptons up to 150 GeV are excluded at 95% CL in the case of a 50 GeV mass-splitting between the sleptons and the LSP.

Exclusion limits are also set for selectrons and smuons separately, considering the same selection (including both dielectron and dimuon events in the likelihood fit) used for the general result. These are shown in Figure 7 for single slepton species $\tilde{e}_R$, $\tilde{e}_L$ and $\tilde{\mu}_L$ along with combined limits for mass-degenerate $\tilde{e}_{L,R}$ and $\tilde{\mu}_{L,R}$. Concerning this last case, parts of the region excluded by this search in the $m(\tilde{\mu}) - m(\tilde{\chi}^0_1)$ plane are compatible with the $(g-2)_\mu$ anomaly for small $\tan\beta$ values [13].

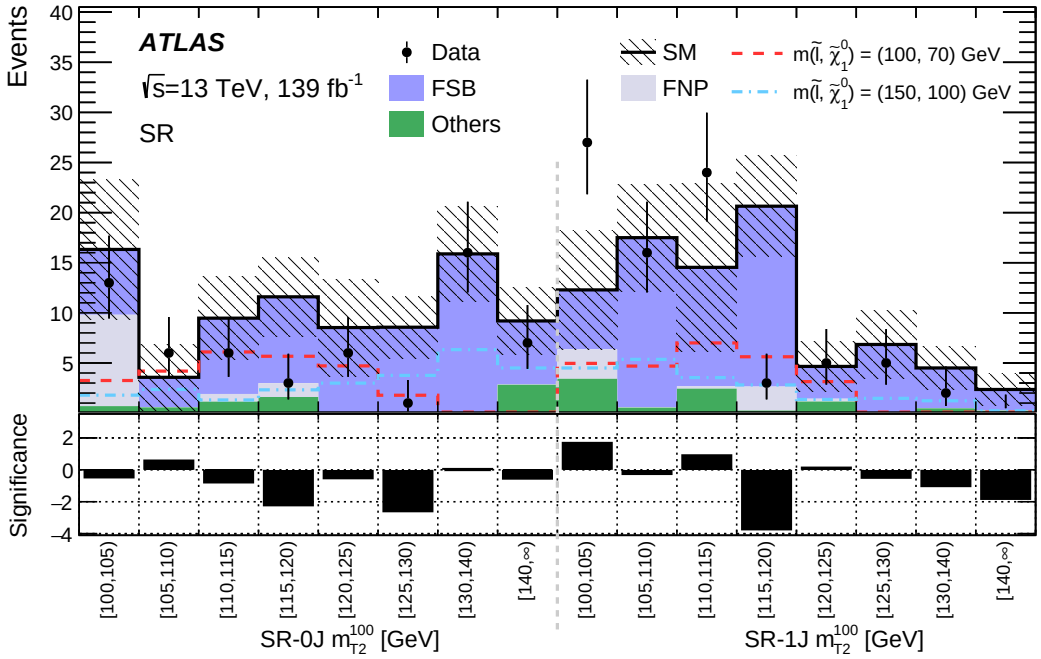

Figure 5: The upper panel shows the observed number of events in each of the binned SRs defined in Table 2, together with the expected SM backgrounds obtained after applying the efficiency correction method to compute the number of expected FSB events. 'Others' include the non-dominant background sources, e.g. $t\bar{t}$+V, Higgs boson and Drell–Yan events. The uncertainty band includes systematic and statistical errors from all sources. The distributions of two signal points with mass splittings $\Delta m(\tilde{\ell}, \tilde{\chi}_1^0) = m(\tilde{\ell}) - m(\tilde{\chi}_1^0)$ of 30 GeV and 50 GeV are overlaid. The lower panel shows the significance as defined in Ref. [121].

Table 10: Observed event yields and predicted background yields for the inclusive SRs defined in Table 2 are reported in the left part of the table, as obtained using the background fit described in Section 9. The right part shows the model-independent upper limits at 95% CL on the observed and expected number of beyond-the-SM events $S^{0.95}_{\text{obs/exp}}$ and on the effective beyond-the-SM cross-section σ^{obs} ($\langle A\epsilon\sigma\rangle^{0.95}_{\text{obs}}$). They were obtained using a fit which includes the SRs, also described in Section 9. The $\pm 1\sigma$ variations of $S^{0.95}_{\text{exp}}$ are provided. The last column shows the p_0-value of the SM-only hypothesis. For SRs where the data yield is smaller than expected, the p_0-value is capped at 0.50.

Signal region [GeV]	Observed	Expected	σ^{obs} [fb]	$S^{0.95}_{\text{obs}}$	$S^{0.95}_{\text{exp}}$	p_0
SR-0J $m_{\text{T2}}^{100} \in [100, \infty)$	58	76 ± 13	0.13	18.3	26^{+10}_{-7}	0.50
SR-0J $m_{\text{T2}}^{100} \in [110, \infty)$	39	58 ± 11	0.09	13.2	21^{+8}_{-6}	0.50
SR-0J $m_{\text{T2}}^{100} \in [120, \infty)$	30	40 ± 8	0.10	13.5	18^{+7}_{-5}	0.50
SR-0J $m_{\text{T2}}^{100} \in [130, \infty)$	23	24 ± 6	0.10	14.2	15^{+6}_{-4}	0.50
SR-0J $m_{\text{T2}}^{100} \in [140, \infty)$	7	9.2 ± 3.4	0.05	7.5	$8.6^{+4}_{-2.5}$	0.50
SR-1J $m_{\text{T2}}^{100} \in [100, \infty)$	82	78 ± 13	0.24	33.5	31^{+11}_{-8}	0.41
SR-1J $m_{\text{T2}}^{100} \in [110, \infty)$	39	50 ± 17	0.17	24.0	28^{+9}_{-7}	0.50
SR-1J $m_{\text{T2}}^{100} \in [120, \infty)$	12	16 ± 5	0.07	9.5	12^{+5}_{-3}	0.50
SR-1J $m_{\text{T2}}^{100} \in [130, \infty)$	2	6.9 ± 2.8	0.03	3.9	$6.1^{+3.0}_{-1.9}$	0.50
SR-1J $m_{\text{T2}}^{100} \in [140, \infty)$	0	2.4 ± 1.6	0.02	2.4	$3.4^{+2.2}_{-1.2}$	0.50

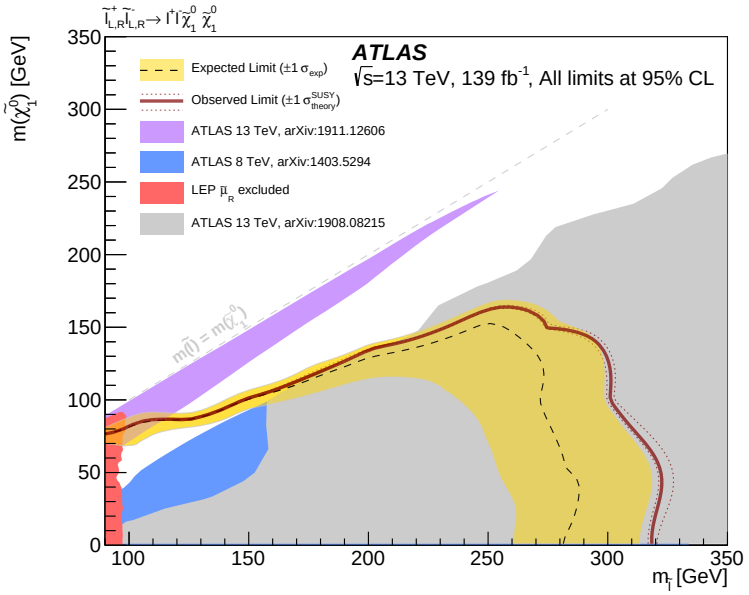

(a)

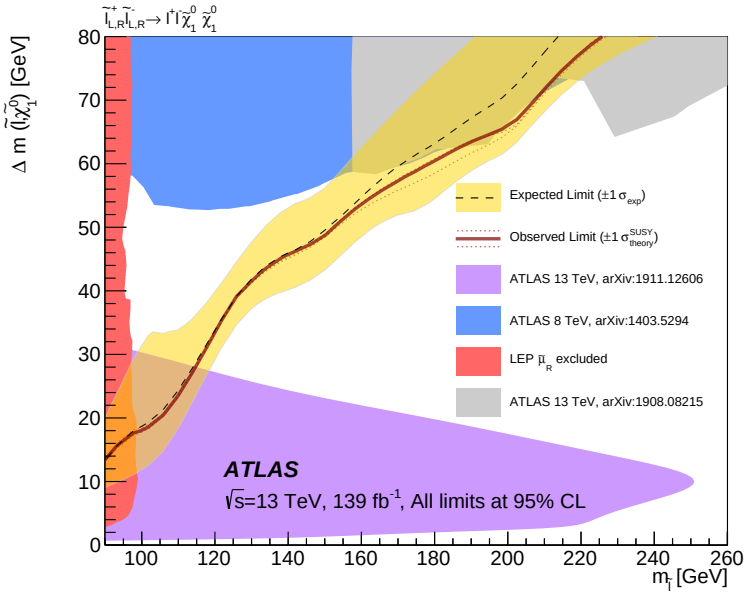

(b)

Figure 6: Observed and expected exclusion limits on SUSY simplified models for slepton-pair production in the (a) $m(\tilde{\ell})$–$m(\tilde{\chi}_1^0)$ and (b) $m(\tilde{\ell})$–$\Delta m(\tilde{\ell}, \tilde{\chi}_1^0)$ planes. Only $\tilde{e}$ and $\tilde{\mu}$ are considered. The observed (solid thick line) and expected (thin dashed line) exclusion contours are shown. The shaded band around the dashed line corresponds to the $\pm 1\sigma$ variations of the expected limit, including all uncertainties except theoretical uncertainties in the signal cross-section. The dotted lines around the observed limit illustrate the change in the observed limit as the nominal signal cross-section is scaled up and down by the theoretical uncertainty. All limits are computed at 95% CL. The observed limits obtained at LEP [122] for $\tilde{\mu}_{\mathrm{R}}$ and by the ATLAS experiment in previous searches are also shown [14, 16, 123].

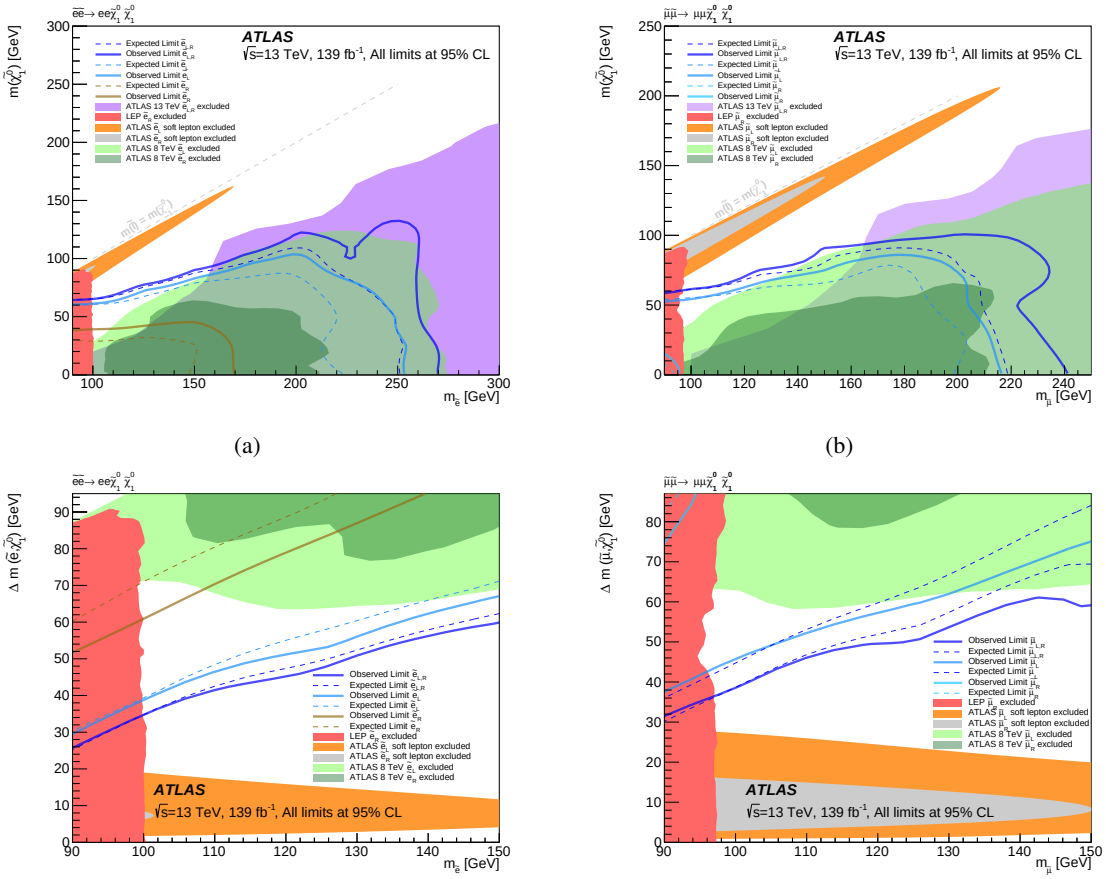

Figure 7: Observed and expected exclusion limits on SUSY simplified models for direct selectron production in the (a) $m(\tilde{e})$–$m(\tilde{\chi}_1^0)$ and (c) $m(\tilde{e})$–$\Delta m(\tilde{e}, \tilde{\chi}_1^0)$ planes, and for direct smuon production in the (b) $m(\tilde{\mu})$–$m(\tilde{\chi}_1^0)$ and (d) $m(\tilde{\mu})$–$\Delta m(\tilde{\mu}, \tilde{\chi}_1^0)$ planes. In figures (a) and (c) the observed (solid thick lines) and expected (dashed lines) exclusion contours are shown for combined $\tilde{e}_{\mathrm{L,R}}$ and for $\tilde{e}_{\mathrm{L}}$ and $\tilde{e}_{\mathrm{R}}$. In figures (b) and (d) the observed (solid thick lines) and expected (dashed lines) exclusion contours are shown for combined $\tilde{\mu}_{\mathrm{L,R}}$ and for $\tilde{\mu}_{\mathrm{L}}$. No unique sensitivity to $\tilde{\mu}_{\mathrm{R}}$ is observed. All limits are computed at 95% CL. The observed limits obtained at LEP [122] and by the ATLAS experiment in previous searches are also shown in the shaded areas [14, 16, 123].

9.2 Results of the chargino search

The predicted numbers of background events, obtained from the results of the background fit in the binned SRs defined in Table 3, are shown together with the observed data in Figure 8. The observed and predicted numbers of background events in the inclusive SRs are shown in Table 11. The model-independent upper limits on the visible signal cross-section σ^{obs}, the observed and expected limits at 95% CL on the number of potential beyond-the-SM events, and the p_0-values for each inclusive SR are also reported. No significant deviations from the SM expectations are observed in any of the SRs considered, as shown in Figure 8.

Exclusion limits at 95% CL are set, using the CL_s prescription, on the masses of the chargino and the LSP. These include the exclusive SRs and the CRs in the simultaneous likelihood fit. The SF and DF SRs are included in the likelihood fit. The exclusion limits are shown in Figure 9. Chargino masses up to 140 GeV are excluded at 95% CL in the case of a mass-splitting between the chargino and neutralino as low as about 100 GeV.

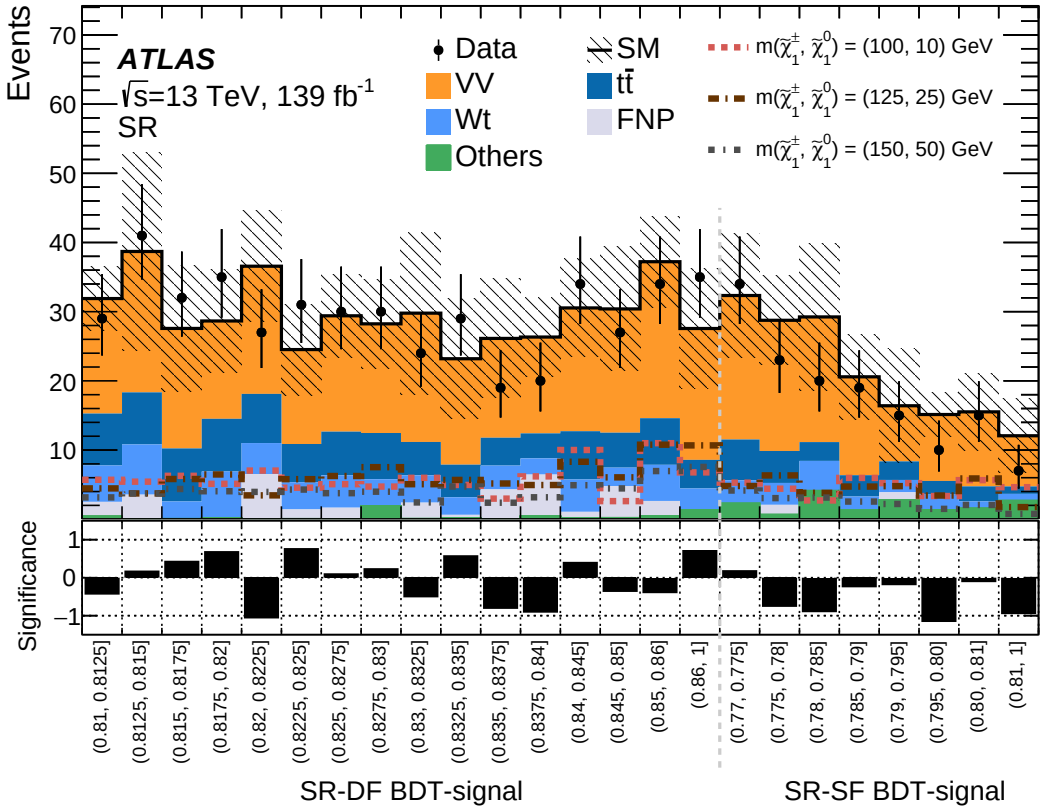

Figure 8: The upper panel shows the observed number of events in the SRs defined in Table 3, together with the expected SM backgrounds obtained after the background fit in the CRs. 'Others' include the non-dominant background sources, e.g. $t\bar{t}+V$, Higgs boson and Drell–Yan events. The uncertainty band includes systematic and statistical errors from all sources. Distributions for three benchmark signal points are overlaid for comparison. The lower panel shows the significance as defined in Ref. [121].

Table 11: Observed event yields and predicted background yields for the inclusive SRs defined in Table 3 are reported in the left part of the table, as obtained using the background fit described in Section 9. The right part shows the model-independent upper limits at 95% CL on the observed and expected numbers of beyond-the-SM events $S^{0.95}_{\text{obs/exp}}$ and on the effective beyond-the-SM cross-section σ^{obs} ($\langle A\epsilon\sigma\rangle^{0.95}_{\text{obs}}$). They were obtained using a fit which includes the SRs, also described in Section 9. The $\pm 1\sigma$ variations of $S^{0.95}_{\text{exp}}$ are provided. The last column shows the p_0-value of the SM-only hypothesis. For SRs where the data yield is smaller than expected, the p_0-value is capped at 0.50.

Signal region	Observed	Expected	σ^{obs} [fb]	$S^{0.95}_{\text{obs}}$	$S^{0.95}_{\text{exp}}$	p_0
SR$^{\text{-DF BDT-signal}\in(0.81,1]}_{\text{-SF BDT-signal}\in(0.77,1]}$	620	630 ± 70	1.20	166.2	$175.1^{+44.9}_{-49.2}$	0.50
SR-DF BDT-signal∈(0.81,1]	477	470 ± 50	0.80	111.0	$108.9^{+43.1}_{-31.1}$	0.47
SR-DF BDT-signal∈(0.82,1]	340	350 ± 40	0.55	76.0	$81.5^{+32.7}_{-22.9}$	0.50
SR-DF BDT-signal∈(0.83,1]	222	231 ± 26	0.38	52.3	$57.8^{+22.9}_{-16.1}$	0.50
SR-DF BDT-signal∈(0.84,1]	130	126 ± 15	0.29	40.0	$37.5^{+15.0}_{-10.5}$	0.41
SR-DF BDT-signal∈(0.85,1]	69	65 ± 10	0.22	30.9	$28.0^{+12.0}_{-8.3}$	0.38
SR-SF BDT-signal∈(0.77,1]	143	167 ± 32	0.47	65.5	$80.6^{+19.4}_{-23.0}$	0.50
SR-SF BDT-signal∈(0.78,1]	86	108 ± 23	0.31	42.8	$53.9^{+18.9}_{-13.6}$	0.50
SR-SF BDT-signal∈(0.79,1]	47	58 ± 15	0.21	28.9	$34.1^{+10.8}_{-7.8}$	0.50
SR-SF BDT-signal∈(0.80,1]	22	28 ± 8	0.10	14.3	$16.8^{+5.9}_{-4.5}$	0.50

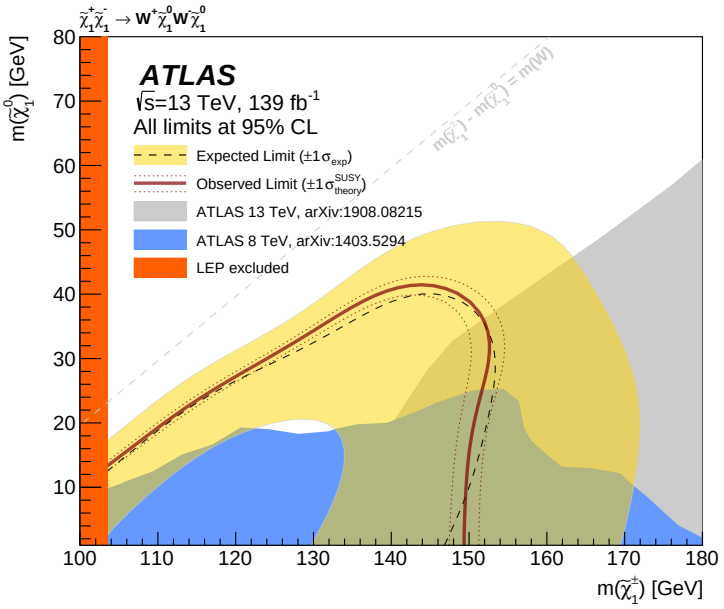

(a)

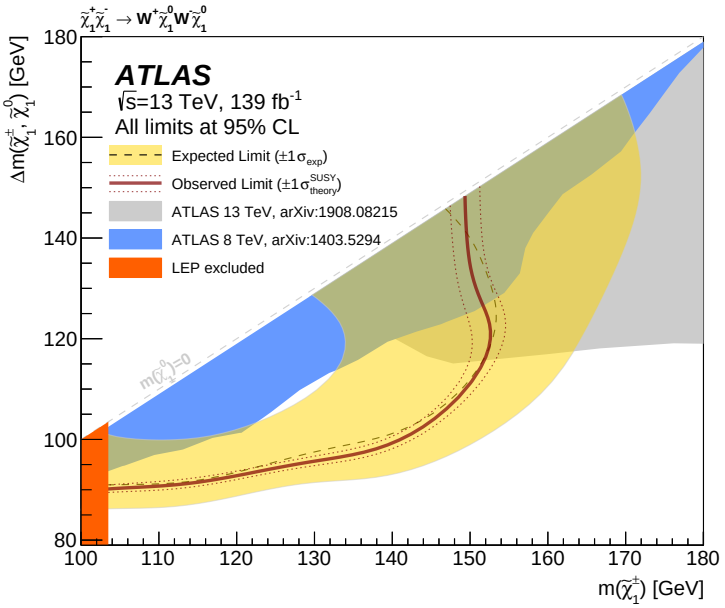

(b)

Figure 9: Observed and expected exclusion limits on SUSY simplified models for chargino-pair production with W-boson-mediated decays in the (a) $m(\tilde{\chi}_1^\pm)$–$m(\tilde{\chi}_1^0)$ and (b) $m(\tilde{\chi}_1^\pm)$–$\Delta m(\tilde{\chi}_1^\pm, \tilde{\chi}_1^0)$ planes. The observed (solid thick line) and expected (thin dashed line) exclusion contours are shown. The shaded band around the dashed line corresponds to the $\pm1\sigma$ variations of the expected limit, including all uncertainties except theoretical uncertainties in the signal cross-section. The dotted lines around the observed limit illustrate the change in the observed limit as the nominal signal cross-section is scaled up and down by the theoretical uncertainty. All limits are computed at 95% CL. The observed limits obtained at LEP [124] and by the ATLAS experiment in previous searches are also shown [14, 16]. In the case of the search performed on ATLAS Run 1 data at $\sqrt{s}$ = 8 TeV [16] no sensitivity was expected for the exclusion in the mass plane.

10 Conclusion

The results of a search for the electroweak production of charginos and sleptons decaying into final states containing two leptons with opposite electric charge and missing transverse momentum are presented. The search uses 139 fb^{-1} of $\sqrt{s}$ = 13 TeV proton–proton collisions collected by the ATLAS experiment at the LHC during Run 2 (2015–2018). Two scenarios are considered: the direct production of slepton pairs, where each slepton decays directly into the lightest neutralino and a lepton, and the production of lightest-chargino pairs, where each decays into a final state with the lightest neutralino plus a lepton via a W-boson decay. The regions with mass differences up to approximately 150 GeV between the sleptons and neutralino and between the chargino and neutralino are explored in these analyses. Models with smuon production with mass differences in this region of the $m(\tilde{\mu})$–$m(\tilde{\chi}_1^0)$ plane are favoured to explain the $(g-2)_\mu$ anomaly for small $\tan\beta$ values. Their decay topologies are similar to those of SM processes, making it challenging to separate signal from background. In order to target these models, a data-driven technique is used to estimate the main backgrounds in the slepton search, and a semi-data-driven approach using CRs to normalize the main backgrounds, classified with a BDT, is used in the chargino search.

The data are found to be consistent with the Standard Model predictions and exclusion limits at 95% CL are set on the masses of relevant supersymmetric particles in each of these scenarios. Slepton masses up to 150 GeV are excluded at 95% CL in the case of a 50 GeV mass-splitting between the sleptons and neutralino, thus surpassing the exclusion limits previously set by the LEP experiments [122], and chargino masses up to 140 GeV are excluded at 95% CL in the case of a mass-splitting between the chargino and neutralino as low as about 100 GeV. Compared to previous analyses for the same scenarios, in the regions with a mass difference up to about 150 GeV between the slepton or chargino and neutralino, the results of these searches extend beyond the exclusion limits previously set at the LHC by ATLAS and CMS [16–21, 23].

References

[1] Y. Golfand and E. Likhtman,
Extension of the Algebra of Poincare Group Generators and Violation of P Invariance,
JETP Lett. **13** (1971) 323, [Pisma Zh. Eksp. Teor. Fiz. **13** (1971) 452].

[2] D. Volkov and V. Akulov, *Is the neutrino a goldstone particle?*, Phys. Lett. B **46** (1973) 109.

[3] J. Wess and B. Zumino, *Supergauge transformations in four dimensions*,
Nucl. Phys. B **70** (1974) 39.

[4] J. Wess and B. Zumino, *Supergauge invariant extension of quantum electrodynamics*,
Nucl. Phys. B **78** (1974) 1.

[5] S. Ferrara and B. Zumino, *Supergauge invariant Yang-Mills theories*, Nucl. Phys. B **79** (1974) 413.

[6] A. Salam and J. Strathdee, *Super-symmetry and non-Abelian gauges*, Phys. Lett. B **51** (1974) 353.

[7] G. R. Farrar and P. Fayet, *Phenomenology of the production, decay, and detection of new hadronic states associated with supersymmetry*, Phys. Lett. B **76** (1978) 575.

[8] H. Goldberg, *Constraint on the Photino Mass from Cosmology*, Phys. Rev. Lett. **50** (1983) 1419,
Erratum: Phys. Rev. Lett. **103** (2009) 099905.

[9] J. Ellis, J. Hagelin, D. V. Nanopoulos, K. A. Olive and M. Srednicki,
Supersymmetric relics from the big bang, Nucl. Phys. B **238** (1984) 453.

[10] G. Bennett et al.,
Final report of the E821 muon anomalous magnetic moment measurement at BNL,
Phys. Rev. D **73** (2006) 072003, arXiv: hep-ex/0602035 [hep-ex].

[11] B. Abi and others (Muon g-2 Collaboration),
Measurement of the Positive Muon Anomalous Magnetic Moment to 0.46 ppm,
Phys. Rev. Lett. **126** (2021) 141801, arXiv: 2104.03281 [hep-ex].

[12] S. Heinemeyer, W. Hollik and G. Weiglein,
Electroweak precision observables in the minimal supersymmetric standard model,
Physics Reports **425** (2006) 265, arXiv: hep-ph/0412214 [hep-ph].

[13] ATLAS Collaboration, *SUSY Summary Plots March 2022*, ATL-PHYS-PUB-2022-013, 2022,
URL: https://cds.cern.ch/record/2805985.

[14] ATLAS Collaboration,
Search for electroweak production of charginos and sleptons decaying into final states with two leptons and missing transverse momentum in $\sqrt{s} = 13$ TeV pp collisions using the ATLAS detector,
Eur. Phys. J. C **80** (2020) 123, arXiv: 1908.08215 [hep-ex].

[15] ATLAS Collaboration,
Object-based missing transverse momentum significance in the ATLAS Detector,
ATLAS-CONF-2018-038, 2018, URL: https://cds.cern.ch/record/2630948.

[16] ATLAS Collaboration,
Search for direct production of charginos, neutralinos and sleptons in final states with two leptons and missing transverse momentum in pp collisions at $\sqrt{s} = 8$ TeV with the ATLAS detector,
JHEP **05** (2014) 071, arXiv: 1403.5294 [hep-ex].

[17] ATLAS Collaboration, *Search for electroweak production of supersymmetric particles in final states with two or three leptons at $\sqrt{s} = 13$ TeV with the ATLAS detector*,
Eur. Phys. J. C **78** (2018) 995, arXiv: 1803.02762 [hep-ex].

[18] CMS Collaboration, *Searches for electroweak production of charginos, neutralinos, and sleptons decaying to leptons and W, Z, and Higgs bosons in pp collisions at 8 TeV*, Eur. Phys. J. C **74** (2014) 3036, arXiv: 1405.7570 [hep-ex].

[19] CMS Collaboration, *Searches for electroweak neutralino and chargino production in channels with Higgs, Z, and W bosons in pp collisions at 8 TeV*, Phys. Rev. D **90** (2014) 092007, arXiv: 1409.3168 [hep-ex].

[20] CMS Collaboration, *Search for electroweak production of charginos and neutralinos in multilepton final states in proton–proton collisions at* $\sqrt{s} = 13$ *TeV*, JHEP **03** (2018) 166, arXiv: 1709.05406 [hep-ex].

[21] CMS Collaboration, *Combined search for electroweak production of charginos and neutralinos in proton–proton collisions at* $\sqrt{s} = 13$ *TeV*, JHEP **03** (2018) 160, arXiv: 1801.03957 [hep-ex].

[22] CMS Collaboration, *Search for supersymmetric partners of electrons and muons in proton–proton collisions at* $\sqrt{s} = 13$ *TeV*, Phys. Lett. B **790** (2019) 140, arXiv: 1806.05264 [hep-ex].

[23] CMS Collaboration, *Searches for pair production of charginos and top squarks in final states with two oppositely charged leptons in proton–proton collisions at* $\sqrt{s} = 13$ *TeV*, JHEP **11** (2018) 079, arXiv: 1807.07799 [hep-ex].

[24] J. Alwall, M.-P. Le, M. Lisanti and J. G. Wacker, *Searching for directly decaying gluinos at the Tevatron*, Phys. Lett. B **666** (2008) 34, arXiv: 0803.0019 [hep-ph].

[25] J. Alwall, P. Schuster and N. Toro, *Simplified models for a first characterization of new physics at the LHC*, Phys. Rev. D **79** (2009) 075020, arXiv: 0810.3921 [hep-ph].

[26] D. Alves et al., *Simplified models for LHC new physics searches*, J. Phys. G **39** (2012) 105005, arXiv: 1105.2838 [hep-ph].

[27] ATLAS Collaboration, *The ATLAS Experiment at the CERN Large Hadron Collider*, JINST **3** (2008) S08003.

[28] ATLAS Collaboration, *ATLAS Insertable B-Layer Technical Design Report*, ATLAS-TDR-19, 2010, URL: https://cds.cern.ch/record/1291633, *ATLAS Insertable B-Layer Technical Design Report Addendum*, ATLAS-TDR-19-ADD-1, 2012, URL: https://cds.cern.ch/record/1451888.

[29] B. Abbott et al., *Production and integration of the ATLAS Insertable B-Layer*, JINST **13** (2018) T05008, arXiv: 1803.00844 [physics.ins-det].

[30] ATLAS Collaboration, *Performance of the ATLAS trigger system in 2015*, Eur. Phys. J. C **77** (2017) 317, arXiv: 1611.09661 [hep-ex].

[31] ATLAS Collaboration, *Operation of the ATLAS trigger system in Run 2*, JINST **15** (2020) P10004, arXiv: 2007.12539 [hep-ex].

[32] ATLAS Collaboration, *The ATLAS Collaboration Software and Firmware*, ATL-SOFT-PUB-2021-001, 2021, URL: https://cds.cern.ch/record/2767187.

[33] ATLAS Collaboration, *ATLAS data quality operations and performance for 2015–2018 data-taking*, JINST **15** (2020) P04003, arXiv: 1911.04632 [physics.ins-det].

[34] ATLAS Collaboration,
Luminosity determination in pp collisions at $\sqrt{s} = 13$ TeV using the ATLAS detector at the LHC,
ATLAS-CONF-2019-021, 2019, URL: https://cds.cern.ch/record/2677054.

[35] G. Avoni et al., *The new LUCID-2 detector for luminosity measurement and monitoring in ATLAS*,
JINST **13** (2018) P07017.

[36] ATLAS Collaboration, *Performance of the ATLAS muon triggers in Run 2*,
JINST **15** (2020) P09015, arXiv: 2004.13447 [hep-ex].

[37] ATLAS Collaboration, *Performance of electron and photon triggers in ATLAS during LHC Run 2*,
Eur. Phys. J. C **80** (2020) 47, arXiv: 1909.00761 [hep-ex].

[38] ATLAS Collaboration, *The ATLAS Simulation Infrastructure*, Eur. Phys. J. C **70** (2010) 823,
arXiv: 1005.4568 [physics.ins-det].

[39] GEANT4 Collaboration, S. Agostinelli et al., *GEANT4 – a simulation toolkit*,
Nucl. Instrum. Meth. A **506** (2003) 250.

[40] T. Sjöstrand, S. Mrenna and P. Z. Skands, *A brief introduction to PYTHIA 8.1*,
Comput. Phys. Commun. **178** (2008) 852, arXiv: 0710.3820 [hep-ph].

[41] D. J. Lange, *The EvtGen particle decay simulation package*,
Nucl. Instrum. Meth. A **462** (2001) 152.

[42] R. D. Ball et al., *Parton distributions with LHC data*, Nucl. Phys. B **867** (2013) 244,
arXiv: 1207.1303 [hep-ph].

[43] ATLAS Collaboration, *The Pythia 8 A3 tune description of ATLAS minimum bias and inelastic measurements incorporating the Donnachie–Landshoff diffractive model*,
ATL-PHYS-PUB-2016-017, 2016, URL: https://cds.cern.ch/record/2206965.

[44] ATLAS Collaboration, *Electron and photon performance measurements with the ATLAS detector using the 2015–2017 LHC proton–proton collision data*, JINST **14** (2019) P12006,
arXiv: 1908.00005 [hep-ex].

[45] ATLAS Collaboration, *Muon reconstruction performance of the ATLAS detector in proton–proton collision data at $\sqrt{s} = 13$ TeV*, Eur. Phys. J. C **76** (2016) 292, arXiv: 1603.05598 [hep-ex].

[46] ATLAS Collaboration, *ATLAS b-jet identification performance and efficiency measurement with $t\bar{t}$ events in pp collisions at $\sqrt{s} = 13$ TeV*, Eur. Phys. J. C **79** (2019) 970,
arXiv: 1907.05120 [hep-ex].

[47] ATLAS Collaboration,
Improvements in $t\bar{t}$ modelling using NLO+PS Monte Carlo generators for Run 2,
ATL-PHYS-PUB-2018-009, 2018, URL: https://cds.cern.ch/record/2630327.

[48] ATLAS Collaboration,
Simulation of top-quark production for the ATLAS experiment at $\sqrt{s} = 13$ TeV,
ATL-PHYS-PUB-2016-004, 2016, URL: https://cds.cern.ch/record/2120417.

[49] ATLAS Collaboration, *Multi-Boson Simulation for 13 TeV ATLAS Analyses*,
ATL-PHYS-PUB-2017-005, 2017, URL: https://cds.cern.ch/record/2261933.

[50] ATLAS Collaboration, *ATLAS simulation of boson plus jets processes in Run 2*,
ATL-PHYS-PUB-2017-006, 2017, URL: https://cds.cern.ch/record/2261937.

[51] S. Frixione, G. Ridolfi and P. Nason,
A positive-weight next-to-leading-order Monte Carlo for heavy flavour hadroproduction,
JHEP **09** (2007) 126, arXiv: 0707.3088 [hep-ph].

[52] P. Nason, *A new method for combining NLO QCD with shower Monte Carlo algorithms*,
JHEP **11** (2004) 040, arXiv: hep-ph/0409146.

[53] S. Frixione, P. Nason and C. Oleari,
Matching NLO QCD computations with parton shower simulations: the POWHEG method,
JHEP **11** (2007) 070, arXiv: 0709.2092 [hep-ph].

[54] S. Alioli, P. Nason, C. Oleari and E. Re, *A general framework for implementing NLO calculations in shower Monte Carlo programs: the POWHEG BOX*, JHEP **06** (2010) 043,
arXiv: 1002.2581 [hep-ph].

[55] T. Sjöstrand et al., *An introduction to PYTHIA 8.2*, Comput. Phys. Commun. **191** (2015) 159,
arXiv: 1410.3012 [hep-ph].

[56] M. Beneke, P. Falgari, S. Klein and C. Schwinn,
Hadronic top-quark pair production with NNLL threshold resummation,
Nucl. Phys. B **855** (2012) 695, arXiv: 1109.1536 [hep-ph].

[57] M. Cacciari, M. Czakon, M. Mangano, A. Mitov and P. Nason, *Top-pair production at hadron colliders with next-to-next-to-leading logarithmic soft-gluon resummation*,
Phys. Lett. B **710** (2012) 612, arXiv: 1111.5869 [hep-ph].

[58] P. Bärnreuther, M. Czakon and A. Mitov, *Percent-Level-Precision Physics at the Tevatron: Next-to-Next-to-Leading Order QCD Corrections to $q\bar{q} \to t\bar{t} + X$*,
Phys. Rev. Lett. **109** (2012) 132001, arXiv: 1204.5201 [hep-ph].

[59] M. Czakon and A. Mitov, *NNLO corrections to top-pair production at hadron colliders: the all-fermionic scattering channels*, JHEP **12** (2012) 054, arXiv: 1207.0236 [hep-ph].

[60] M. Czakon and A. Mitov,
NNLO corrections to top pair production at hadron colliders: the quark-gluon reaction,
JHEP **01** (2013) 080, arXiv: 1210.6832 [hep-ph].

[61] M. Czakon, P. Fiedler and A. Mitov,
Total Top-Quark Pair-Production Cross Section at Hadron Colliders Through $O(\alpha_S^4)$,
Phys. Rev. Lett. **110** (2013) 252004, arXiv: 1303.6254 [hep-ph].

[62] M. Czakon and A. Mitov,
Top++: A program for the calculation of the top-pair cross-section at hadron colliders,
Comput. Phys. Commun. **185** (2014) 2930, arXiv: 1112.5675 [hep-ph].

[63] ATLAS Collaboration, *ATLAS Pythia 8 tunes to 7 TeV data*, ATL-PHYS-PUB-2014-021, 2014,
URL: https://cds.cern.ch/record/1966419.

[64] R. D. Ball et al., *Parton distributions for the LHC run II*, JHEP **04** (2015) 040,
arXiv: 1410.8849 [hep-ph].

[65] E. Re,
Single-top Wt-channel production matched with parton showers using the POWHEG method,
Eur. Phys. J. C **71** (2011) 1547, arXiv: 1009.2450 [hep-ph].

[66] N. Kidonakis,
Two-loop soft anomalous dimensions for single top quark associated production with a W^- or H^-,
Phys. Rev. D **82** (2010) 054018, arXiv: 1005.4451 [hep-ph].

[67] N. Kidonakis, 'Top Quark Production', *Proceedings, Helmholtz International Summer School on Physics of Heavy Quarks and Hadrons (HQ 2013)* (JINR, Dubna, Russia, 15th–28th July 2013) 139, arXiv: 1311.0283 [hep-ph].

[68] E. Bothmann et al., *Event generation with Sherpa 2.2*, SciPost Phys. **7** (2019) 034, arXiv: 1905.09127 [hep-ph].

[69] T. Gleisberg and S. Höche, *Comix, a new matrix element generator*, JHEP **12** (2008) 039, arXiv: 0808.3674 [hep-ph].

[70] S. Schumann and F. Krauss, *A parton shower algorithm based on Catani–Seymour dipole factorisation*, JHEP **03** (2008) 038, arXiv: 0709.1027 [hep-ph].

[71] S. Höche, F. Krauss, M. Schönherr and F. Siegert, *A critical appraisal of NLO+PS matching methods*, JHEP **09** (2012) 049, arXiv: 1111.1220 [hep-ph].

[72] S. Höche, F. Krauss, M. Schönherr and F. Siegert, *QCD matrix elements + parton showers. The NLO case*, JHEP **04** (2013) 027, arXiv: 1207.5030 [hep-ph].

[73] S. Catani, F. Krauss, B. R. Webber and R. Kuhn, *QCD Matrix Elements + Parton Showers*, JHEP **11** (2001) 063, arXiv: hep-ph/0109231.

[74] S. Höche, F. Krauss, S. Schumann and F. Siegert, *QCD matrix elements and truncated showers*, JHEP **05** (2009) 053, arXiv: 0903.1219 [hep-ph].

[75] J. Alwall et al., *The automated computation of tree-level and next-to-leading order differential cross sections, and their matching to parton shower simulations*, JHEP **07** (2014) 079, arXiv: 1405.0301 [hep-ph].

[76] H. B. Hartanto, B. Jäger, L. Reina and D. Wackeroth, *Higgs boson production in association with top quarks in the POWHEG BOX*, Phys. Rev. D **91** (2015) 094003, arXiv: 1501.04498 [hep-ph].

[77] C. Anastasiou, L. Dixon, K. Melnikov and F. Petriello, *High-precision QCD at hadron colliders: Electroweak gauge boson rapidity distributions at next-to-next-to leading order*, Phys. Rev. D **69** (2004) 094008, arXiv: hep-ph/0312266.

[78] S. Alioli, P. Nason, C. Oleari and E. Re, *A general framework for implementing NLO calculations in shower Monte Carlo programs: the POWHEG BOX*, JHEP **06** (2010) 043, arXiv: 1002.2581 [hep-ph].

[79] K. Hamilton, P. Nason, E. Re and G. Zanderighi, *NNLOPS simulation of Higgs boson production*, JHEP **10** (2013) 222, arXiv: 1309.0017 [hep-ph].

[80] K. Hamilton, P. Nason and G. Zanderighi, *Finite quark-mass effects in the NNLOPS POWHEG+MiNLO Higgs generator*, JHEP **05** (2015) 140, arXiv: 1501.04637 [hep-ph].

[81] K. Hamilton, P. Nason and G. Zanderighi, *MINLO: multi-scale improved NLO*, JHEP **10** (2012) 155, arXiv: 1206.3572 [hep-ph].

[82] J. M. Campbell et al., *NLO Higgs boson production plus one and two jets using the POWHEG BOX, MadGraph4 and MCFM*, JHEP **07** (2012) 092, arXiv: 1202.5475 [hep-ph].

[83] K. Hamilton, P. Nason, C. Oleari and G. Zanderighi, *Merging H/W/Z + 0 and 1 jet at NLO with no merging scale: a path to parton shower + NNLO matching*, JHEP **05** (2013) 082, arXiv: 1212.4504 [hep-ph].

[84] S. Catani and M. Grazzini, *Next-to-Next-to-Leading-Order Subtraction Formalism in Hadron Collisions and its Application to Higgs-boson Production at the Large Hadron Collider*, Phys. Rev. Lett. **98** (2007) 222002, arXiv: hep-ph/0703012 [hep-ph].

[85] ATLAS Collaboration, *Measurement of the Z/γ^* boson transverse momentum distribution in pp collisions at $\sqrt{s} = 7$ TeV with the ATLAS detector*, JHEP **09** (2014) 145, arXiv: 1406.3660 [hep-ex].

[86] J. Butterworth et al., *PDF4LHC recommendations for LHC Run II*, J. Phys. G **43** (2016) 023001, arXiv: 1510.03865 [hep-ph].

[87] J. Alwall et al., *MadGraph/MadEvent v4: The New Web Generation*, JHEP **09** (2007) 028, arXiv: 0706.2334 [hep-ph].

[88] P. Artoisenet, R. Frederix, O. Mattelaer and R. Rietkerk, *Automatic spin-entangled decays of heavy resonances in Monte Carlo simulations*, JHEP **03** (2013) 015, arXiv: 1212.3460 [hep-ph].

[89] L. Lönnblad and S. Prestel, *Merging multi-leg NLO matrix elements with parton showers*, JHEP **03** (2013) 166, arXiv: 1211.7278 [hep-ph].

[90] J. Debove, B. Fuks and M. Klasen, *Threshold resummation for gaugino pair production at hadron colliders*, Nucl. Phys. B **842** (2011) 51, arXiv: 1005.2909 [hep-ph].

[91] B. Fuks, M. Klasen, D. R. Lamprea and M. Rothering, *Gaugino production in proton-proton collisions at a center-of-mass energy of 8 TeV*, JHEP **10** (2012) 081, arXiv: 1207.2159 [hep-ph].

[92] B. Fuks, M. Klasen, D. R. Lamprea and M. Rothering, *Precision predictions for electroweak superpartner production at hadron colliders with* RESUMMINO, Eur. Phys. J. C **73** (2013) 2480, arXiv: 1304.0790 [hep-ph].

[93] J. Fiaschi and M. Klasen, *Neutralino-chargino pair production at NLO+NLL with resummation-improved parton density functions for LHC Run II*, Phys. Rev. D **98** (2018) 055014, arXiv: 1805.11322 [hep-ph].

[94] G. Bozzi, B. Fuks and M. Klasen, *Threshold resummation for slepton-pair production at hadron colliders*, Nucl. Phys. B **777** (2007) 157, arXiv: hep-ph/0701202 [hep-ph].

[95] B. Fuks, M. Klasen, D. R. Lamprea and M. Rothering, *Revisiting slepton pair production at the Large Hadron Collider*, JHEP **01** (2014) 168, arXiv: 1310.2621 [hep-ph].

[96] J. Fiaschi and M. Klasen, *Slepton pair production at the LHC in NLO+NLL with resummation-improved parton densities*, JHEP **03** (2018) 094, arXiv: 1801.10357 [hep-ph].

[97] C. Borschensky et al., *Squark and gluino production cross sections in pp collisions at $\sqrt{s} = 13, 14, 33$ and 100 TeV*, Eur. Phys. J. C **74** (2014) 3174, arXiv: 1407.5066 [hep-ph].

[98] ATLAS Collaboration,
Jet reconstruction and performance using particle flow with the ATLAS Detector,
Eur. Phys. J. C **77** (2017) 466, arXiv: 1703.10485 [hep-ex].

[99] M. Cacciari, G. P. Salam and G. Soyez, *The anti-k_t jet clustering algorithm*, JHEP **04** (2008) 063, arXiv: 0802.1189 [hep-ph].

[100] M. Cacciari, G. P. Salam and G. Soyez, *FastJet user manual*, Eur. Phys. J. C **72** (2012) 1896, arXiv: 1111.6097 [hep-ph].

[101] ATLAS Collaboration, *Jet energy scale measurements and their systematic uncertainties in proton–proton collisions at $\sqrt{s}$ = 13 TeV with the ATLAS detector*, Phys. Rev. D **96** (2017) 072002, arXiv: 1703.09665 [hep-ex].

[102] ATLAS Collaboration, *Tagging and suppression of pileup jets with the ATLAS detector*, ATLAS-CONF-2014-018, 2014, URL: https://cds.cern.ch/record/1700870.

[103] ATLAS Collaboration,
Selection of jets produced in 13 *TeV proton–proton collisions with the ATLAS detector*,
ATLAS-CONF-2015-029, 2015, URL: https://cds.cern.ch/record/2037702.

[104] ATLAS Collaboration, *Performance of pile-up mitigation techniques for jets in pp collisions at $\sqrt{s}$ = 8 TeV using the ATLAS detector*, Eur. Phys. J. C **76** (2016) 581, arXiv: 1510.03823 [hep-ex].

[105] ATLAS Collaboration, *Performance of missing transverse momentum reconstruction with the ATLAS detector using proton–proton collisions at $\sqrt{s}$ = 13 TeV*, Eur. Phys. J. C **78** (2018) 903, arXiv: 1802.08168 [hep-ex].

[106] C. G. Lester and D. J. Summers,
Measuring masses of semi-invisibly decaying particles pair produced at hadron colliders,
Phys. Lett. B **463** (1999) 99, arXiv: hep-ph/9906349.

[107] A. Barr, C. G. Lester and P. Stephens, *A variable for measuring masses at hadron colliders when missing energy is expected; m_{T2}: the truth behind the glamour*, J. Phys. G **29** (2003) 2343, arXiv: hep-ph/0304226.

[108] A. Barr, *Measuring slepton spin at the LHC*, JHEP **02** (2006) 042, arXiv: hep-ph/0511115.

[109] G. Ke et al., *LightGBM: A Highly Efficient Gradient Boosting Decision Tree*,
NIPS'17 (2017) 3149.

[110] ATLAS Collaboration, *Estimation of non-prompt and fake lepton backgrounds in final states with top quarks produced in proton–proton collisions at $\sqrt{s}$ = 8 TeV with the ATLAS Detector*, ATLAS-CONF-2014-058, 2014, URL: https://cds.cern.ch/record/1951336.

[111] ATLAS Collaboration, *Jet energy scale and resolution measured in proton–proton collisions at $\sqrt{s}$ = 13 TeV with the ATLAS detector*, Eur. Phys. J. C **81** (2020) 689, arXiv: 2007.02645 [hep-ex].

[112] ATLAS Collaboration, *Determination of jet calibration and energy resolution in proton–proton collisions at $\sqrt{s}$ = 8 TeV using the ATLAS detector*, Eur. Phys. J. C **80** (2020) 1104, arXiv: 1910.04482 [hep-ex].

[113] E. Bothmann, M. Schönherr and S. Schumann,
Reweighting QCD matrix-element and parton-shower calculations, Eur. Phys. J. C **76** (2016) 590, arXiv: 1606.08753 [hep-ph].

[114] M. Bähr et al., *Herwig++ physics and manual*, Eur. Phys. J. C **58** (2008) 639, arXiv: 0803.0883 [hep-ph].

[115] J. Bellm et al., *Herwig 7.0/Herwig++ 3.0 release note*, Eur. Phys. J. C **76** (2016) 196, arXiv: 1512.01178 [hep-ph].

[116] ATLAS Collaboration, *Studies on top-quark Monte Carlo modelling with Sherpa and MG5_aMC@NLO*, ATL-PHYS-PUB-2017-007, 2017, URL: https://cds.cern.ch/record/2261938.

[117] S. Frixione, E. Laenen, P. Motylinski, C. White and B. R. Webber, *Single-top hadroproduction in association with a W boson*, JHEP **07** (2008) 029, arXiv: 0805.3067 [hep-ph].

[118] ATLAS Collaboration, *Studies on top-quark Monte Carlo modelling for Top2016*, ATL-PHYS-PUB-2016-020, 2016, URL: https://cds.cern.ch/record/2216168.

[119] M. Baak et al., *HistFitter software framework for statistical data analysis*, Eur. Phys. J. C **75** (2015) 153, arXiv: 1410.1280 [hep-ex].

[120] A. L. Read, *Presentation of search results: the CL_S technique*, J. Phys. G **28** (2002) 2693.

[121] R. D. Cousins, J. T. Linnemann and J. Tucker, *Evaluation of three methods for calculating statistical significance when incorporating a systematic uncertainty into a test of the background-only hypothesis for a Poisson process*, Nucl. Instrum. Meth. A **595** (2008) 480, arXiv: physics/0702156 [physics.data-an].

[122] LEPSUSYWG, ALEPH, DELPHI, L3, OPAL Collaborations, *Combined LEP Chargino Results, up to 208 GeV for large m0*, LEPSUSYWG/04-01.1 (2004), URL: http://lepsusy.web.cern.ch/lepsusy/www/sleptons_summer04/slep_final.html.

[123] ATLAS Collaboration, *Searches for electroweak production of supersymmetric particles with compressed mass spectra in $\sqrt{s} = 13$ TeV pp collisions with the ATLAS detector*, Phys. Rev. D **101** (2020) 052005, arXiv: 1911.12606 [hep-ex].

[124] LEPSUSYWG, ALEPH, DELPHI, L3, OPAL Collaborations, *Combined LEP Selectron/Smuon/Stau Results, 183-208 GeV*, LEPSUSYWG/01-03.1 (2001), URL: http://lepsusy.web.cern.ch/lepsusy/www/inos_moriond01/charginos_pub.html.